IEEE Journal of Microwaves

Received 19 October 2021; revised 14 November 2021; accepted 26 November 2021. Date of publication 22 December 2021; date of current version 7 January 2022.

Digital Object Identifier 10.1109/JMW.2021.3131856

Tunable Bandpass Filters With Reconfigurable Symmetric Transmission Zeros on Real or Imaginary Axis

WENTAO LIN [1] (Graduate Student Member, IEEE), PING ZHAO [2], TAE-HAK LEE [3] (Member, IEEE), TAIJUN LIU[4] (Senior Member, IEEE), JEAN-JACQUES LAURIN [1] (Senior Member, IEEE), AND KE WU [1] (Fellow, IEEE)

(Regular Paper)

[1]Poly-Grames Research Center, Department of Electrical Engineering, Polytechnique Montréal (University of Montreal), Montréal, QC H3T 1J4, Canada
[2]National Key Laboratory of Antennas and Microwave Technology, Xidian University, Xi'an, Shaanxi 710071, China
[3]Department of Electronics, Yuhan University, Gyeonggi-do 14780, Republic of Korea
[4]Faculty of Electrical Engineering and Computer Science, Ningbo University, Ningbo 315211, China

CORRESPONDING AUTHOR: Ke Wu (e-mail: ke.wu@polymtl.ca).

This work was supported in part by the Natural Science and Engineering Research Council (NSERC)-Huawei Industrial Research Chair Program.

ABSTRACT This paper introduces a coupling matrix synthesis method tailored for a class of tunable bandpass filters (BPFs) with reconfigurable filtering characteristics. The filter has symmetric transmission zeros (TZs) which can be reconfigured on the real or imaginary axis of the complex plane. Different filtering characteristics can be obtained by merely tuning resonant frequencies of certain resonators. The frequency tuning and reconfigurable states of the filter can be achieved simultaneously. The synthesis procedure mainly includes three steps. First, a transversal coupling matrix is synthesized according to the design specifications of one of the reconfigurable states. Second, the matrix is transformed to an intermediate configuration, in which some of the coupling coefficients on the mainline couplings are designated as the key coefficients. Tuning these key coefficients alone can change the locations of TZs to realize reconfigurable filtering characteristics. In this intermediate configuration, the coupling matrix is optimized based on the synthesized values to make all reconfigurable filter states meet their design requirements. Finally, the key coefficients are rotated to the diagonal entries of the coupling matrix, so that reconfigurable TZs are realized by merely tuning the resonant frequencies of certain resonators. The reconfigurable mechanism and the maximum number of TZs under different filter orders are investigated in detail for a variety of coupling diagrams. Two synthesis examples are presented to show the novel reconfigurable filter optimization procedure. For experimental verification, a fourth-order tunable BPF with a pair of reconfigurable symmetric TZs was fabricated and measured. The filter states with TZs on the real or imaginary axis of the complex plane can be switched solely by tuning resonant frequencies, which validates the proposed synthesis approach of tunable filters.

INDEX TERMS Coupling matrix, dual-mode, reconfigurable, transmission zeros, tunable bandpass filter.

I. INTRODUCTION

Tunable filters are important alternatives to traditional filter banks thanks to their wide frequency coverage, flexible reconfigurable capability, and compact size. They play an ever-increasing critical role in emerging terrestrial and space wireless communication systems in response to the trendy development of multi-network convergences and multi-function applications such as space-air-ground integrated network, cognitive radio, and software-defined radio (SDR). Different methods for designing tunable filters with transmission zeros (TZs) on the complex plane have been proposed in recent decades [1]–[15]. Symmetric TZs on the appropriate positions of the real axis of the complex plane can improve the in-band group delay response, which are usually created by an in-phase cross-coupling in a cascaded quadruplet (CQ) topology [16]–[21]. On the other hand, symmetric TZs on the

imaginary axis of the complex plane can improve near-skirt selectivity, which can also be generated by the CQ coupling diagram but with a negative cross-coupling [22]. For the physical realization of cross-coupled filters, positive couplings are usually realized as inductive coupling irises, whereas negative couplings are created through different realizations, which have been widely investigated [8], [22]–[26]. For example, a capacitive coupling probe in waveguide structures [8] or balanced microstrip lines with a pair of metallic via-holes in a substrate integrated waveguide (SIW) structure [22] can introduce a negative coupling. Multilayered topologies [23] and [24], and higher-order modes with properly designed coupling irises [25] and [26] can also produce negative couplings.

It is well-known that the phases of different paths in cross-coupled topologies determine the type of TZs. Therefore, reconfigurable filtering characteristics can be realized by reversing the signs of cross-couplings. In this way, a versatile internal coupling circuit design that can tune coupling coefficients from positive to negative was presented [6], [27]–[29]. In [6] and [27], an appropriate combination of magnetic and electric couplings was realized by soldered varactor diodes. Two inter-resonator coupling structures, namely the negative microstrip line and the positive inductive iris, are integrated in [28]. Dual-mode resonators with perturbation technology were reported to introduce a coupling phase reversal equivalently [29]. However, there are three drawbacks in the previous designs of tunable bandpass filters. First, all these approaches require relatively complicated circuit structures, which demand for time-consuming simulation and high precision fabrication. Second, the tuning range of internal coupling coefficients is limited by the tuning elements designed to control the coupling strength. It may not be able to completely cover the required tuning range of the filter in question. Third, the internal coupling coefficients and the resonant frequencies are controlled independently, which would increase the number of tuning elements. Although numerous efforts and attempts related to tunable bandpass filters involving the relocation of TZs have been presented, theoretical guidance on reconfiguring symmetric TZs on the complex plane has not been reported or discussed so far.

In this paper, an approach of synthesis for tunable bandpass filters with reconfigurable symmetric TZs is proposed. The complex internal coupling structure design can be replaced by simple inductive coupling irises, which is theoretically interpreted through coupling matrix rotations. At the same time, the symmetric TZs reconfigurability on the real or imaginary axis of the complex plane can be managed together with a center frequency control by merely tuning the resonant frequencies to decrease the number of tuning elements. Besides, the reconfigurable mechanism and the maximum number of controllable TZs under various coupling diagrams are investigated in detail for different filter orders.

The subsequent sections are organized as follows. The proposed synthesis procedure of tunable bandpass filters is introduced and explained in Section II. The optimization steps are provided in Section III. Two synthesis examples are presented in Section IV to show how to implement the optimization steps. In Section V, a fourth-order tunable bandpass filter prototype is fabricated and measured to experimentally validate the proposed method. Finally, the conclusion is drawn in Section VI.

II. SYNTHESIS PROCEDURE OF TUNABLE FILTERS

In this section, the synthesis procedure of tunable filters is detailed and discussed. Realizing reconfigurable symmetric TZs on the complex plane is the primary concern in this work. The synthesis procedure can be divided into five steps:

1) Synthesize a normalized coupling matrix. A transversal coupling matrix can be synthesized according to the design specifications for realizing the generalized Chebyshev filtering characteristics [30].
2) Transform the coupling matrix. The transversal coupling matrix is first transformed to a folded canonical form. Then the folded coupling matrix is further rotated to an intermediate cascaded topology, where some mainline couplings are chosen as the key coefficients. Tuning these key coefficients alone can realize reconfigurable filtering characteristics. How to choose key coefficients depends on the cascaded blocks in the intermediate topology, which will be explained in the following sections.
3) Make the cross and mainline couplings positive. If a cross-coupling is negative, multiplying the whole row and column by -1 would reverse its sign. Subsequently, this process is repeated and applied to the mainline couplings except for those key coefficients.
4) Optimize the coupling matrix. The initial coupling matrix is synthesized based on one possible set of TZs. It may not produce acceptable performances for other reconfigurable filter states, which are obtained by sweeping the key coefficients. All the other coupling matrix entries need to be optimized to make different reconfigurable filter states meet the requirements. Details about the optimization are given in Section III.
5) Rotate the key coefficients to the diagonal entries of the coupling matrix. As a result, the effect of tuning the key coupling coefficients is equivalently achieved by shifting the resonant frequencies of certain resonators. Originally, all the resonators must be tuned to shift the center frequency of the filter. Therefore, after the key coefficients are transformed to diagonal positions of the coupling matrix, reconfigurable filter states can be realized without increasing the number of tuning elements.

After introducing the synthesis procedure, the reconfigurable mechanism and the maximum number of controllable TZs for different filter orders will be investigated in detail. Two sub-topologies are introduced to explain how to reconfigure the state of a filter, as shown in Fig. 1. The quad and hexa sub-topology can control one and two pairs of TZs, respectively, according to the positions of key coefficients which are marked with red solid lines. However, there seems

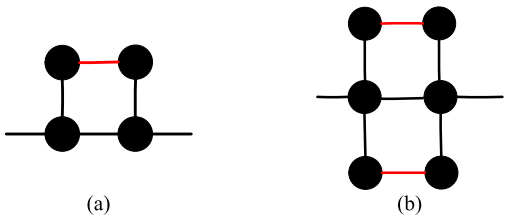

FIGURE 1. Sub-topology in the intermediate topology. (a) Quad sub-topology. (b) Hexa sub-topology. Black circles: resonaors. Black solid lines: constant couplings. Red solid lines: constant couplings chosen for these key coefficients.

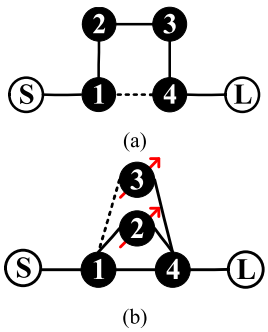

FIGURE 2. Coupling topology of a fourth-order filter. (a) Folded configuration after coupling matrix synthesis. (b) Quad-section configuration after eliminating M_{23}. Black circles: resonators. Hollow circles: terminals. Solid line segments: positive coupling. Dash line segments: negative coupling. Red arrows: resonant frequencies shifting.

to be no regular pattern of coupling matrix rotations to transfer a folded configuration to a sub-topology-based configuration. Therefore, each order needs to be considered individually. The different coupling diagrams can be classified into three categories, namely quad-section, hexa-section, and mixed-section.

A. MULTIPATH COUPLING DIAGRAM OF QUAD-SECTION

The quad sub-topology is shown in Fig. 1(a). Every four resonators can be employed to control a pair of symmetric TZs in the quad sub-topology. The minimum order to realize the quad-section topology is four. The coupling diagram is shown in Fig. 2(a) and the corresponding coupling matrix takes the following form

$$M = \begin{bmatrix} 0 & M_{S1} & 0 & 0 & 0 & 0 \\ M_{S1} & 0 & M_{12} & 0 & M_{14} & 0 \\ 0 & M_{12} & 0 & M_{23} & 0 & 0 \\ 0 & 0 & M_{23} & 0 & M_{34} & 0 \\ 0 & M_{14} & 0 & M_{34} & 0 & M_{4L} \\ 0 & 0 & 0 & 0 & M_{4L} & 0 \end{bmatrix}. \tag{1}$$

The fourth-order configuration is a special case since the folded configuration is the same as the quadruplet configuration. If the sign of M_{14} is negative, the second row and column are then multiplied by -1 to make it positive. Similar procedures can be applied to make mainline couplings M_{S1} and M_{12} positive. Eventually, the only possible negative value in the coupling matrix is M_{23}.

TABLE 1. Relationship Between Value of M_{23} and Location of TZs in the Fourth-Order Filter

Value of M_{23}	Solution of s	Location of TZs
$M_{23} > 0$	Pure real	On the real axis
$M_{23} < 0$	Pure imaginary	On the imaginary axis

The locations of TZs should satisfy the condition whereby the equation of S_{21} is equal to 0 [31].

$$S_{21} = \frac{P(s)}{\varepsilon E(s)} = 2\sqrt{R_S R_L}[y]_{N1} = 0, \tag{2}$$

where $P(s)$ and $E(s)$ are two polynomials with respect to the complex frequency variable s. ε is a real factor to normalize the highest-order coefficients in the two polynomials. R_S and R_L are the reference impedance of source and load, respectively. [y'] is the nodal admittance matrix. From (2), we can find that the positions of TZs should satisfy the following condition,

$$s^2 + M_{23}\left(M_{23} - \frac{M_{12}M_{34}}{M_{14}}\right) = 0. \tag{3}$$

s has a pair of pure real or imaginary roots depending on whether M_{23} is positive or negative. In the generalized Chebyshev filters, $M_{12}^2/M_{14} \gg M_{23}$, which means that the TZs can be switched between pure real and pure imaginary, as summarized in Table 1. The key coefficient M_{23} changes its sign to reconfigure filtering characteristics, but the other reconfigured states may not meet the design requirements because the coupling matrix is initially synthesized based on one possible set of TZs. Hence, optimization is necessary, which will be explained in detail in Section III.

At last, the coupling matrix rotations [16]–[18] can be applied to rotate the key coefficient M_{23} in (4).

$$M^{(n+1)} = R \cdot M^{(n)} \cdot R^T \quad (n = 1, 2, 3, ..), \tag{4}$$

where the new matrix $M^{(n+1)}$ has the same eigenvalues and eigenvectors as $M^{(n)}$. The rotation matrix R is defined by the pivot $[i, j]$, and the rotation angle θ_r. R^T is the transpose of R. In R, all the diagonal entries are 1 and off-diagonal entries are 0, except for $R_{ii} = R_{jj} = \cos\theta_r$ and $R_{ji} = -R_{ij} = \sin\theta_r$ ($i, j \neq 1$ or $N+2$, and $i \neq j$).

The rotation angle θ_{r1} can be calculated through

$$\theta_{r1} = \frac{1}{2}\tan^{-1}\left(\frac{2M_{i,j}}{M_{j,j} - M_{i,i}}\right). \tag{5}$$

Substituting $M_{22} = M_{33} = 0$ into (5) yields $\theta_{r1} = \pm\pi/4$. After applying (4) to the coupling matrix in (1), the coupling matrix becomes

$$M = \begin{bmatrix} 0 & M_{S1} & 0 & 0 & 0 & 0 \\ M_{S1} & 0 & \frac{M_{12}}{\sqrt{2}} & -\frac{M_{12}}{\sqrt{2}} & M_{14} & 0 \\ 0 & \frac{M_{12}}{\sqrt{2}} & M_{23} & 0 & \frac{M_{34}}{\sqrt{2}} & 0 \\ 0 & -\frac{M_{12}}{\sqrt{2}} & 0 & -M_{23} & \frac{M_{34}}{\sqrt{2}} & 0 \\ 0 & M_{14} & \frac{M_{34}}{\sqrt{2}} & \frac{M_{34}}{\sqrt{2}} & 0 & M_{S1} \\ 0 & 0 & 0 & 0 & M_{S1} & 0 \end{bmatrix}. \tag{6}$$

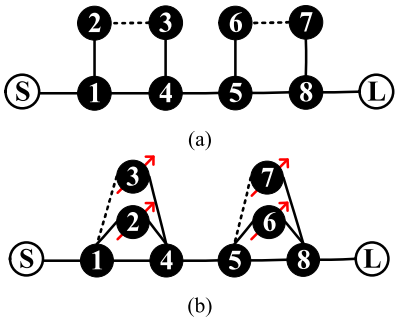

FIGURE 3. Coupling topologies of eighth-order filter. (a) Cascaded quadruplet (CQ) configuration after coupling matrix rotations. (b) Final configuration after eliminating M_{23} and M_{67}.

This step aims to eliminate the coupling between resonators 2 and 3. At the same time, it creates non-zero elements on the diagonal of the coupling matrix, which can control the location of TZs. In this process, the reconfiguration mechanism of the filter is transformed from internal coupling coefficient tuning to resonant frequency tuning. The quad-section topology corresponding to the coupling matrix in (6) is depicted in Fig. 2(b). Tuning the resonant frequencies of resonator 2 and resonator 3 can reconfigure the state of the filter. This is the important step to realize center frequencies tuning and reconfigurable responses at the same time by merely tuning resonant frequencies.

To independently control two pairs of TZs, cascaded quad-section topologies can be used with a minimum filter order of eight. Similar to the fourth-order topology, the eighth-order filter can be synthesized in a folded configuration with cross-couplings M_{36} and M_{27}, then the topology can be transformed into a CQ configuration by coupling matrix rotations. The detailed procedures of rotations are given in [16]. The CQ topology is drawn in Fig. 3(a) with the corresponding coupling matrix, shown as

$$M = \begin{bmatrix} 0 & M_{S1} & 0 & 0 & 0 & 0 & 0 & 0 & 0 & 0 \\ M_{S1} & 0 & M_{12} & 0 & M_{14} & 0 & 0 & 0 & 0 & 0 \\ 0 & M_{12} & 0 & M_{23} & 0 & 0 & 0 & 0 & 0 & 0 \\ 0 & 0 & M_{23} & 0 & M_{34} & 0 & 0 & 0 & 0 & 0 \\ 0 & M_{14} & 0 & M_{34} & 0 & M_{45} & 0 & 0 & 0 & 0 \\ 0 & 0 & 0 & 0 & M_{45} & 0 & M_{56} & 0 & M_{58} & 0 \\ 0 & 0 & 0 & 0 & 0 & M_{56} & 0 & M_{67} & 0 & 0 \\ 0 & 0 & 0 & 0 & 0 & 0 & M_{67} & 0 & M_{78} & 0 \\ 0 & 0 & 0 & 0 & 0 & M_{58} & 0 & M_{78} & 0 & M_{8L} \\ 0 & 0 & 0 & 0 & 0 & 0 & 0 & 0 & M_{8L} & 0 \end{bmatrix}. \tag{7}$$

In (7), all the coefficients can be made positive by the aforementioned procedures, except for the possible negative values of M_{23} and M_{67}. The TZs satisfy the following condition based on (2).

$$\begin{aligned} &\left[M_{14}s^2 + M_{23}\left(M_{14}M_{23} - M_{12}M_{34}\right)\right] \\ &*\left[M_{58}s^2 + M_{67}\left(M_{67}M_{58} - M_{56}M_{78}\right)\right] = 0. \end{aligned} \tag{8}$$

The values of $M_{23}, M_{12}, M_{14}, M_{34}$ and $M_{67}, M_{56}, M_{58}, M_{78}$, shown in blue and red in (7), respectively, can individually control a pair of TZs. M_{23} and M_{67} are chosen as the key coefficients to control the locations of TZs. For instance, if M_{23} or M_{67} is positive, the solutions of s are pure real because the mainline couplings are larger than those cross-couplings in the generalized Chebyshev filters (i.e., $M_{14}M_{23}$-$M_{12}M_{34} < 0$, $M_{67}M_{58}$-$M_{56}M_{78} < 0$).

The final step is to annihilate the coupling coefficients M_{23} and M_{67} in (4) and (5). The two key coefficients are rotated to the diagonal entries of the coupling matrix with the same absolute values but opposite signs, shown as

$$M = \begin{bmatrix} 0 & M_{S1} & 0 & 0 & 0 & 0 & 0 & 0 & 0 & 0 \\ M_{S1} & 0 & \frac{M_{12}}{\sqrt{2}} & -\frac{M_{12}}{\sqrt{2}} & M_{14} & 0 & 0 & 0 & 0 & 0 \\ 0 & \frac{M_{12}}{\sqrt{2}} & M_{23} & 0 & \frac{M_{34}}{\sqrt{2}} & 0 & 0 & 0 & 0 & 0 \\ 0 & -\frac{M_{12}}{\sqrt{2}} & 0 & -M_{23} & \frac{M_{34}}{\sqrt{2}} & 0 & 0 & 0 & 0 & 0 \\ 0 & M_{14} & \frac{M_{34}}{\sqrt{2}} & \frac{M_{34}}{\sqrt{2}} & 0 & M_{45} & 0 & 0 & 0 & 0 \\ 0 & 0 & 0 & 0 & M_{45} & 0 & \frac{M_{56}}{\sqrt{2}} & -\frac{M_{56}}{\sqrt{2}} & M_{58} & 0 \\ 0 & 0 & 0 & 0 & 0 & \frac{M_{56}}{\sqrt{2}} & M_{67} & 0 & \frac{M_{78}}{\sqrt{2}} & 0 \\ 0 & 0 & 0 & 0 & 0 & -\frac{M_{56}}{\sqrt{2}} & 0 & -M_{67} & \frac{M_{78}}{\sqrt{2}} & 0 \\ 0 & 0 & 0 & 0 & 0 & M_{58} & \frac{M_{78}}{\sqrt{2}} & \frac{M_{78}}{\sqrt{2}} & 0 & M_{8L} \\ 0 & 0 & 0 & 0 & 0 & 0 & 0 & 0 & M_{8L} & 0 \end{bmatrix}. \tag{9}$$

The coefficients corresponding to the resonant frequencies, i.e., resonators 2 and 3, resonators 6 and 7, can independently control a pair of symmetric TZs. Hence, four (22) different states in total can be achieved in the 8$^{\text{th}}$-order filter. (6) and (9) show that the topology in Fig. 3(b) consists of two cascaded quad-section configurations, and their matrix coefficients are asymmetric about the principal diagonal.

In a 12$^{\text{th}}$-order filter, the same synthesis technique can be applied. However, the coupling matrix rotations become much more complicated because three cascaded quad-sections need to be reconfigured. A detailed procedure is described in the Appendix, and three pairs of TZs can be independently controlled by tuning resonant frequencies. There are eight (23) different states in terms of the reconfigured locations of TZs. The pivots and rotation angles for the 12$^{\text{th}}$-order filter of cascaded quad-section topology are listed in Table 2. It is worth pointing out that a pair of symmetric TZs can be controlled by every four resonators in filters of other orders ($\geq$4). For example, 7$^{\text{th}}$-order and 9$^{\text{th}}$-order topology can have one and two pairs of independently controlled TZs, respectively. Their target topologies can be chosen with reference to the synthesis procedures of 4$^{\text{th}}$-order and 8$^{\text{th}}$-order topologies.

B. MULTIPATH COUPLING DIAGRAM OF HEXA-SECTION

The hexa sub-topology is shown in Fig. 1(b). Compared with a quad sub-topology, a hexa sub-topology can control more TZs, but its tuning mechanism is more complicated. In a hexa-section, the six resonators can dependently control two pairs

TABLE 2. Pivots and Rotation Angles for 12th Filter Order With Quad-Section Topology

Degree N	Rotation No. R	Pivot [i, j]	$\theta r=\tan^{-1}(k\, M_{u1,u2}/M_{v1,v2})$					Annihilated elements
			u1	u2	v1	v2	k	
12	1	[4,8]					+1	
	2	[5,7]					+1	
	3	[6,8]	5	8	5	6	-1	M_{58}
	4	[7,9]	6	9	6	7	-1	M_{49}, M_{69}
	5	[8,10]	7	10	7	8	-1	M_{310}, M_{710}
	6	[9,11]	8	11	8	9	-1	M_{811}
	7	[4,6]					+1	
	8	[5,7]	4	7	4	5	-1	M_{47}
	9	[3,5]	3	6	5	6	+1	M_{36}, M_{38}
	10	[2,4]	2	5	4	5	+1	M_{25}
	11							M_{23}, M_{67}, M_{1011}

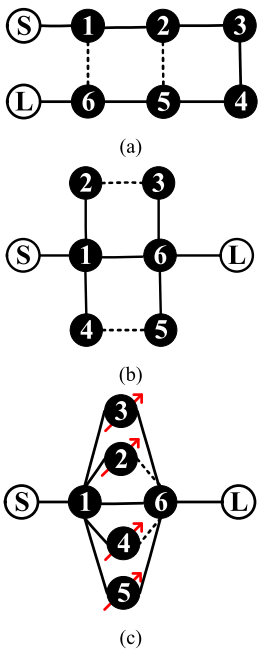

FIGURE 4. Coupling topologies of sixth-order filter. (a) Folded configuration after coupling matrix synthesis. (b) Six-section configuration after coupling matrix rotations. (c) Final configuration after eliminating M_{23} and M_{45}.

of symmetric TZs. The synthesis procedure of a hexa-section also starts from a folded topology, as shown in Fig. 4(a). The transformation of the folded coupling matrix to a hexa-section form [16], [32] is illustrated in Fig. 5. Here, all the nonzero entries are indicated with 'X'; the newly created entries are represented by '⊗'; and the eliminated entries are marked as '◯'. The first rotation angle θ_1 has an unknown value with the pivot [2], [4]. This operation aims to eliminate M_{25} and M_{34} simultaneously in the next step. The second rotation uses an angle θ_2 with the pivot [3], [5]. θ_2 can be calculated by (10).

$$\theta_2 = -\tan^{-1}\left(\frac{M_{j,k}}{M_{i,k}}\right), \tag{10}$$

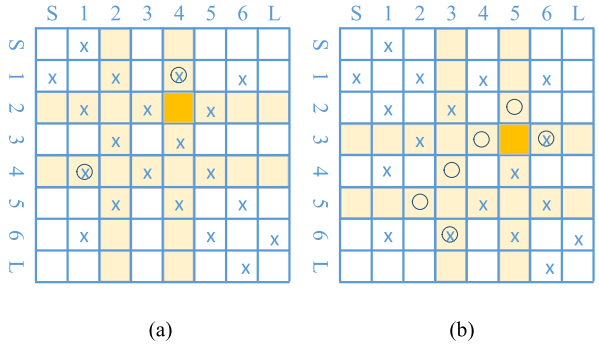

FIGURE 5. Coupling matrix rotations from a folded topology to a hexa-section topology. (a) Rotation with unknown angle θ_1. (b) Rotation to eliminate M_{25}, M_{34} simultaneously. '◯' denotes eliminated coefficients after rotations. '⊗' denotes newly created coefficients after rotations. 'X' denotes nonzero coupling coefficients.

where $i = 3, j = 5, k = 2$. This step eliminates M_{25} and M_{34} simultaneously. To determine θ_1, coupling coefficients in rows i and j and columns i and j are calculated since only they will be changed by the rotation. In the following derivations, the simplified notations are adopted: $c_1 = \cos\theta_1$, $t_1 = \tan\theta_1$, and $s_1 = \sin\theta_1$. After the coupling matrix rotations, M'_{ij} represents the matrix coefficient after the first rotation, *etc*. The details are shown below:

1) *AFTER THE FIRST ROTATION:*

$$\begin{aligned}
M'_{12} &= c_1 M_{12} \\
M'_{23} &= c_1 M_{23} - s_1 M_{34} \\
M'_{34} &= s_1 M_{23} + c_1 M_{34} \\
M'_{45} &= s_1 M_{25} + c_1 M_{45} \\
M'_{25} &= c_1 M_{25} - s_1 M_{45} \\
M'_{14} &= s_1 M_{12}
\end{aligned} \tag{11}$$

2) *AFTER THE SECOND ROTATION:*

$$\begin{aligned}
M''_{25} &= s_2 M'_{23} + c_2 M'_{25} \\
M''_{34} &= c_2 M'_{34} - s_2 M'_{45}
\end{aligned} \tag{12}$$

To enforce M''_{25} and M''_{34} in (12) to be zero simultaneously, t_2 is set to be $\frac{-M'_{25}}{M'_{23}}$ or $\frac{M'_{34}}{M'_{45}}$. Then, substituting into (11), t_1 can be expressed as follows:

$$\begin{aligned}
&t_1^2\,(-M_{23}M_{34} - M_{25}M_{45}) \\
&+ t_1\left(M_{23}^2 - M_{34}^2 + M_{25}^2 - M_{45}^2\right) \\
&+ (M_{23}M_{34} + M_{25}M_{45}) = 0.
\end{aligned} \tag{13}$$

As all the coefficients in (13) are known at the beginning, t_1 can be solved. The topology after the rotations is shown in Fig. 4(b). The locations of TZs can be calculated with (3) and

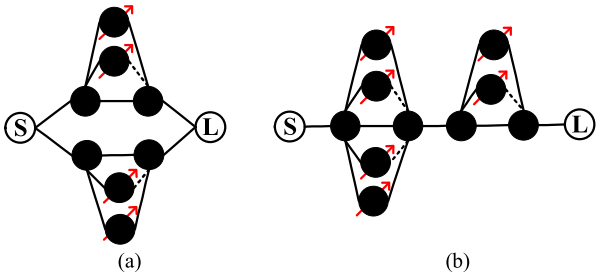

FIGURE 6. Possible coupling topologies of mixed-section. (a) Two quad-section topologies in parallel. (b) Cascading of a quad-section topology and a hexa-section topology.

the simplified equation is

$$M_{16}\left(s^2+M_{45}^2\right)\left(s^2+M_{23}^2\right)-M_{12}M_{36}M_{23}\left(s^2+M_{45}^2\right) - M_{14}M_{56}M_{45}\left(s^2+M_{23}^2\right)=0. \quad (14)$$

It is difficult to directly obtain the relationship between the coupling coefficients and the locations of TZs from (14). However, two points are clear. First, the solutions of s can be pure real, pure imaginary, and conjugate complex values. Only the solutions of pure real and pure imaginary values (on the axes) will be discussed in this paper. Second, the solutions of s can be controlled by the key coefficients M_{45} and M_{23} to change the locations of TZs. Theoretically, there are up to four different states, but the total number of states is limited by the coupling values in (14).

Finally, through (4) and (5), coupling coefficients M_{45} and M_{23} are rotated to the diagonal entries of the coupling matrix with coefficients M_{22}, M_{33}, M_{44}, and M_{55}. In other words, the reconfigurable filtering characteristics will be realized by tuning the resonant frequencies of resonators 2, 3, 4, and 5. The final hexa-section topology is shown in Fig. 4(c).

The 12th-order filter can have two cascaded hexa-sections. Each hexa-section can control two pairs of TZs independently. Hence, the 12th-order filter has up to sixteen (24) different states. The coupling matrix transformation from the folded topology to the cascaded hexa-section topology is very complicated. 21 rotations are needed to reconfigure the coupling matrix. The pivots and the rotation angles of the hexa-section topology are listed in Table 3 for different filter orders. Like the quad-section topology, each pair of symmetric TZs can be controlled using similar coupling matrix rotations. For instance, the 7th-order topology can control two pairs of TZs referring to the 6th-order topology's rotation.

C. MULTIPATH COUPLING DIAGRAM OF MIXED-SECTION

As discussed above, the quad-section and hexa-section can be used as building blocks to control one and two pairs of symmetric TZs, respectively. They can be connected in different ways to extend the diversity of responses and realizations. In Fig. 6, some coupling topologies consisting of different sub-sections are illustrated to realize different characteristics.

TABLE 3. Pivots and Rotation Angles for Hexa-Section Topology for Different Filter Orders

Degree N	Rotation No. R	Pivot [i,j]	θr=tan^{-1}(k $M_{u1,u2}/M_{v1,v2}$)					Annihilated elements
			u1	u2	v1	v2	k	
6	1	[2,4]						
	2	[3,5]	2	5	2	3	-1	M_{25}, M_{34}
	3							M_{23}, M_{45}
12	1	[3,9]					+1	
	2	[4,8]					+1	
	3	[5,7]					+1	
	4	[6,8]	5	8	5	6	-1	M_{58}
	5	[7,9]	6	9	6	7	-1	M_{49}, M_{69}
	6	[8,10]	7	10	7	8	-1	M_{310}, M_{710}
	7	[9,11]	8	11	8	9	-1	M_{211}, M_{811}
	8	[3,7]					+1	
	9	[4,6]					+1	
	10	[5,7]	4	7	4	5	-1	M_{47}
	11	[6,8]	5	8	5	6	-1	M_{58}, M_{38}
	12	[7,9]	6	9	6	7	-1	M_{29}, M_{69}
	13	[8,10]	7	10	7	8	-1	M_{710}
	14	[9,11]					+1	M_{912}
	15	[3,5]					+1	
	16	[2,6]	2	7	6	7	+1	M_{27}, M_{36}
	17	[2,4]					+1	
	18	[3,5]	2	5	2	3	-1	M_{25}, M_{34}
	19	[8,10]					+1	
	20	[9,11]	8	11	8	9	-1	M_{811}, M_{910}
	21							M_{23}, M_{45}, M_{89}, M_{1011}

In Fig. 6(a), two quad-sections in parallel have the same responses as the cascaded quartet topology, though their coupling diagrams are different, leading to better flexibility in the physical design. Additionally, the quad-section topology is cascaded with the hexa-section topology to control three pairs of TZs in total, as shown in Fig. 6(b), which is a hybrid form between the pure quad- and hexa-section topologies. The mixed-section topology provides a tradeoff between these two topologies to realize the same number of symmetric TZs with a lower order of the filter.

III. OPTIMIZATION

Since the initial coupling matrix is synthesized based on one possible set of TZs, the performance of other reconfigurable states, especially, the return loss level, may deteriorate when the key coefficients change their signs or values. Hence, the initial coupling matrix needs to be optimized to make a tradeoff among all states with respect to the design specifications. The optimization procedure mainly contains four steps:

Step 1: Change the value of the key coefficient to reconfigure filter characteristics.

Following the procedure described in Section II, a coupling matrix with an intermediate topology has been synthesized.

The positions of key coefficients are given in Fig. 1 to reconfigure the locations of TZs. The final values of the key coefficients are determined to optimally satisfy the system requirements on the reconfigurable filter, such as return loss level, group delay flatness, and out-of-band rejection, *etc*. For example, the following cost function can be used to evaluate the filter performance in terms of the in-band return loss and the stopband rejection as:

$$C = \max\left\{dB\left(S_{11}\right) \text{ in passband}, -r_{in}\right\} + w \cdot \max\left\{dB\left(S_{21}\right) \text{ in stopband}, -r_{out}\right\}, \quad (15)$$

where r_{in} and r_{out} are the prescribed in-band return loss level and stopband rejection level, respectively. w is a predefined weight factor. The reconfigurable states are determined with a set of key coefficient values that can minimize C. Note that the initial coupling matrix should be synthesized for the reconfigurable states with the most challenging specifications.

Step 2: Check whether the performances of all reconfigurable states meet design requirements. If not, synthesize a coupling matrix for each reconfigurable state.

Usually, it is the return loss levels of reconfigurable states that do not meet design specifications. If the performances of some reconfigurable states are not satisfactory, then for each state, resynthesize a coupling matrix based on the calculated locations of TZs of that state. So if there are N reconfigurable states, there will be N synthesized coupling matrices. Note that all the N coupling matrices should be reconfigured to the same intermediate coupling topology as the initial matrix obtained in step 1.

Step 3: Fine-tune the coefficients to obtain the final coupling matrix.

N coupling matrices are synthesized in step 2. However, we can use only one final coupling matrix to guide and enable the physical realization of the filter. The final coupling matrix should make a compromise among all the reconfigurable states. Therefore, each of its coefficients is fine-tuned within the range whose the lower and upper bounds are determined by the minimum and maximum values in the corresponding positions of the N coupling matrices obtained in step 2. Direct optimization of all the coefficients to construct a new coupling matrix that can give satisfactory performance for all reconfigurable states is time-consuming due to too many optimization variables. Therefore, we introduce a simple approach to derive the final coupling matrix. The final coupling matrix M_{F} is determined by the weighted sum of all the matrices obtained in step 2 as follows,

$$M_F = a_1 * M_1 + a_2 * M_2 \ldots + a_i * M_i \ldots + a_N * M_N, \quad (16)$$

where a_i is the weight factor for the coupling matrix M_i, and M_i is the synthesized coupling matrix for the i^{th} reconfigurable state. The values of a_i satisfy $a_1 + a_2 + \ldots + a_i + \ldots + a_N = 1$, and $a_i \geq 0$.

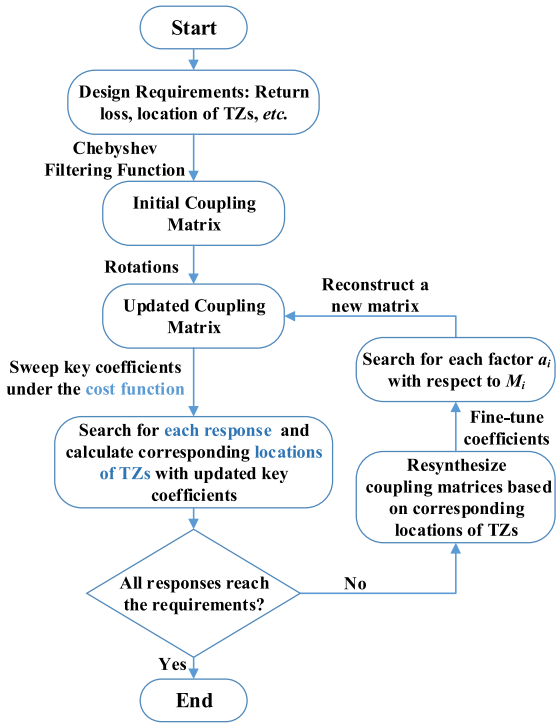

FIGURE 7. Flowchart for coupling matrix optimization.

With (16), the optimization variables are converted from the non-zero coefficients in the coupling matrix to the weight factors a_1 to a_N. In this way, the number of optimization variables can be reduced because the number of states N is often smaller than the total number of non-zero coefficients in the coupling matrix. The optimal solution stemmed from the optimization procedure can be found because it is a brute-force method by sweeping all the variables in the corresponding dynamic range. An appropriate set of weight factors can be determined by an exhaustive parameter sweep to make all the reconfigurable states of M_{F} have close return loss levels. Then, M_{F} gives the best performance of all states. According to our experience, it is not necessary to optimize all the a_i's values. Usually, the lower and upper bounds of all the coupling coefficients are determined by only two matrices, whose TZs are all on the real axis and the imaginary axis of the complex plane, respectively. Satisfactory results can be obtained if we set all the a_i's zero, except the two for the above two matrices. Then the number of non-zero weight factors is decreased to two to reduce the amount of calculation.

Step 4: Repeat steps 1 to 3 until all the states meet the design requirements.

If sweeping a_i in (16) fails to make all reconfigurable states meet the design requirements, we can resynthesize the coupling matrices with a higher return loss level at the beginning. Then repeating steps 1 to 3, until all the states meet the design specifications. The flow chart of coupling matrix optimization is shown in Fig. 7. The whole procedure can be programmed

$$\begin{bmatrix} 0 & 1.0989 & 0 & 0 & 0 & 0 \\ 1.0989 & 0 & 0.9894 & 0 & 0.1927 & 0 \\ 0 & 0.9894 & 0 & 0.6526 & 0 & 0 \\ 0 & 0 & 0.6526 & 0 & 0.9894 & 0 \\ 0 & 0.1927 & 0 & 0.9894 & 0 & 1.0989 \\ 0 & 0 & 0 & 0 & 1.0989 & 0 \end{bmatrix}$$

(a)

$$\begin{bmatrix} 0 & 1.0937 & 0 & 0 & 0 & 0 \\ 1.0937 & 0 & 0.9476 & 0 & 0.1590 & 0 \\ 0 & 0.9476 & 0 & -0.7980 & 0 & 0 \\ 0 & 0 & -0.7980 & 0 & 0.9476 & 0 \\ 0 & 0.1590 & 0 & 0.9476 & 0 & 1.0937 \\ 0 & 0 & 0 & 0 & 1.0937 & 0 \end{bmatrix}$$

(b)

$$\begin{bmatrix} 0 & 1.0953 & 0 & 0 & 0 & 0 \\ 1.0953 & 0 & 0.9601 & 0 & 0.1691 & 0 \\ 0 & 0.9601 & 0 & -0.3628 & 0 & 0 \\ 0 & 0 & -0.3628 & 0 & 0.9601 & 0 \\ 0 & 0.1691 & 0 & 0.9601 & 0 & 1.0953 \\ 0 & 0 & 0 & 0 & 1.0953 & 0 \end{bmatrix}$$

(c)

$$\begin{bmatrix} 0 & 1.0953 & 0 & 0 & 0 & 0 \\ 1.0953 & 0 & 0.6789 & -0.6789 & 0.1691 & 0 \\ 0 & 0.6789 & -0.8181 & 0 & 0.6789 & 0 \\ 0 & -0.6789 & 0 & 0.8181 & 0.6789 & 0 \\ 0 & 0.1691 & 0.6789 & 0.6789 & 0 & 1.0953 \\ 0 & 0 & 0 & 0 & 1.0953 & 0 \end{bmatrix}$$

(d)

FIGURE 8. Coupling matrix of a fourth-order filter obtained by an analytical synthesized procedure. (a) Simplified coupling matrix with folded topology synthesized from the Chebyshev filtering function. (b) The second matrix synthesized from the Chebyshev filtering function with the return loss of 23 dB and the TZs of ±2.2681j rad/s. (c) The optimized matrix with weight factor of 0.3 and 0.7 according to the matrices in (a) and (b), respectively. (d) The final matrix after rotating coefficient M_{23}, where $M_{23} = -0.8181$ in the matrix before rotation.

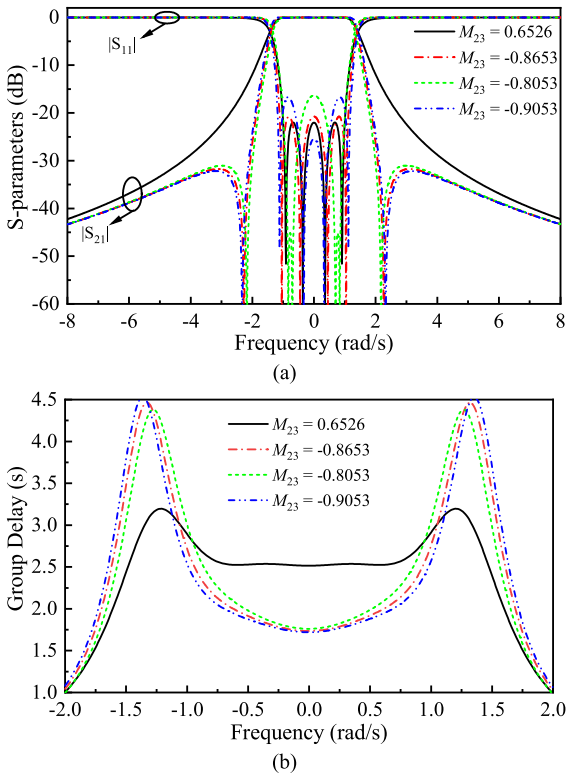

FIGURE 9. The responses by sweeping the key coefficients M_{23}. (a) S-parameters. (b) Group delay.

using scientific computational tools, such as MATLAB, to optimize the final matrix.

In the following sections, two synthesis and one design examples are illustrated to show how to implement the optimization steps.

IV. SYNTHESIS EXAMPLES

A. A FOURTH-ORDER FILTER WITH TWO RECONFIGURABLE STATES

A fourth-order reconfigurable filter with one pair of TZs is taken as the first example. The return loss levels of both reconfigurable states should be better than 22 dB. One of the states gives group delay equalization over 70% of the passband.

Step 1: The initial matrix is synthesized from the Chebyshev filtering function with the prescribed TZs at ±1.7 rad/s and a return loss of 22 dB. The initial coupling matrix is shown in Fig. 8(a).

As analyzed in Section II, the pair of TZs can be controlled by tuning the key coefficient M_{23} in the quad sub-topology. As seen in (3) and Table 1, there are two reconfigurable states corresponding to a positive and a negative value of M_{23}. The coupling matrix with a positive M_{23} (i.e., 0.6526) is initially synthesized from the Chebyshev filtering function, as shown in Fig. 8(a). The location of TZs is placed on the real axis of the complex plane in this state. The other state can be found by sweeping the negative values of M_{23} to minimize the cost function (16). The S-parameters under different values of M_{23} are plotted in Fig. 9(a). It is seen that the in-band return loss level is affected by the value of the key coefficient M_{23}. The best return loss level of the second reconfigurable state is 20.7453 dB, which is obtained by a negative M_{23} (i.e., −0.8653). The positions of TZs on the imaginary axis of the complex plane are also changed with different negative values of M_{23}, which can be calculated by (3). Substituting $M_{23} = -0.8653$ into (3), the values of TZs are ±2.2681j rad/s.

At the same time, the group delay flatness is also affected by tuning M_{23}, as shown in Fig. 9(b). When the location of TZs is switched from the real axis to the imaginary axis of the complex plane, the near-skirt selectivity of the filter becomes better, but the in-band group delay flatness becomes worse.

Step 2: It is seen that the state with TZs on the imaginary axis of the complex plane has deteriorated return loss performance. Hence, the coupling matrix needs to be resynthesized for the second reconfigurable state. In general, the return loss levels of reconfigured filter states will be slightly lower than that of the initially synthesized state. Therefore, the return loss level used in the analytical synthesis procedure can be chosen slightly higher than the required level. In this example, the coupling matrix is resynthesized based

TABLE 4. Performance of Two States After Fine-Tuning the Key Coefficient and Locations of TZs

No. of states	M_{23}	Return loss (dB)	Locations of TZs
1	0.6411	22.3975	±1.7561
2	-0.8181	22.2752	±2.2647j

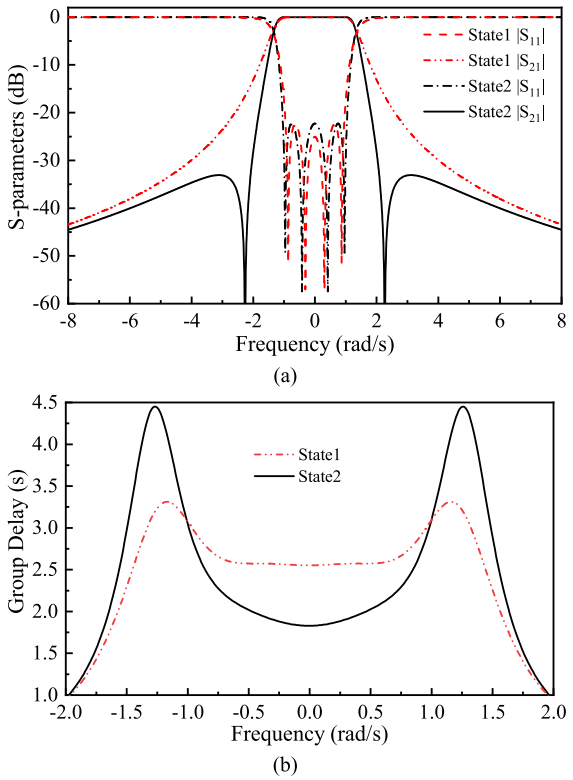

FIGURE 10. The responses of two states for the fourth-order filter after optimization. (a) Magnitude of S-parameters. (b) Group delay. State1: TZs on the real axis of the complex plane. State2: TZs on the imaginary axis of the complex plane.

on the TZs of ±2.2681j rad/s and the return loss of 23 dB, in order to meet the return loss requirement of 22 dB. The synthesized coupling matrix is given in Fig. 8(b). The next step is adjusting all the coefficients in the coupling matrix.

Step 3: Implementing the simplified adjustment-based method, the final matrix is given in Fig. 8(c). It is obtained with the weight factor of $a_1 = 0.3$ and $a_2 = 0.7$ according to the matrices in Fig. 8(a) and Fig. 8(b), respectively. Repeating steps 1 to 2 with the matrix in Fig. 8(c), the return loss level and the locations of TZs are updated in Table 4. Finally, the return loss levels of both states are better than 22 dB. The magnitude and group delay responses of both states are shown in Fig. 10(a) and (b), respectively. The group delay equalization of the first state with TZs on the real axis of the complex plane is over 70% of the passband.

With the coupling matrix in the intermediate topology, the states can be reconfigured by merely tuning the key coefficient M_{23}. The last step is to rotate the intermediate coupling matrix using (4) and (5). The resultant matrix is given in Fig. 8(d),

TABLE 5. Coefficients of S-Parameter Polynomials

s^i, i=	$E(s)$	$F(s)$	$P(s)$
0	0.1343	0.0095	36
1	0.7437	0	0
2	2.1265	0.2794	13
3	3.9646	0	0
4	5.5134	1.3268	1
5	5.4780	0	
6	4.4576	2.0506	
7	2.1941	0	
8	1	1	
$\varepsilon = 268.6451$,		$\varepsilon_R = 1$	

which is eventually transformed to the quad-section based topology. Now different reconfigurable filter states can be realized by tuning the resonant frequencies of resonators 2 and 3 without modifying any other coefficient. The center frequency tuning and the reconfigurable states controlling can be realized by tuning all resonant frequencies simultaneously.

B. AN EIGHTH-ORDER FILTER WITH FOUR RECONFIGURALBE STATES

An eighth-order reconfigurable filter with two pairs of TZs is taken as the second example. In this example, the return loss of all states should be better than 23 dB, and one of the states gives out-of-band rejection better than 85 dB when the normalized frequency > 2 rad/s.

Step 1: The initial values of TZs are ±2j and ±3j rad/s, and the return loss level is 23 dB. The transfer and reflection characteristics can be synthesized from the generalized Chebyshev filtering function. The coefficients of the polynomials are given in Table 5. The simplified coupling matrix in the folded topology is obtained and shown in Fig. 11(a). Rotating the folded topology to the cascaded CQ topology has been introduced in [16]. The first rotating angle is calculated that $tan\theta = -0.0926$ or -0.0354. After completing the matrix rotations, the matrix in the CQ topology is shown in Fig. 11(b). As can be seen, all the coefficients are positive except for M_{23} and M_{67}.

As analyzed in Section II, these two pairs of TZs can be independently controlled by sweeping the key coefficients M_{23} and M_{67} in the quad sub-topology. There are four reconfigurable states based on the locations of TZs. In this case, it can be seen from (8) that these four states are obtained by positive and negative values of the key coefficients M_{23} and M_{67} (positive M_{23}, positive M_{67}; positive M_{23}, negative M_{67}; negative M_{23}, positive M_{67}; negative M_{23}, negative M_{67}). The coupling matrix with negative M_{23} and negative M_{67} is given in Fig. 11(b). The coupling matrices corresponding to the other three states can be found by sweeping the key coefficients M_{23} and M_{67} to minimize the cost function (16). The four reconfigurable states are summarized in Table 4. As can be seen, the return loss level of states 2 to 4 are slightly worse and do not meet the design requirements.

$$\begin{bmatrix}
0 & 1.0474 & 0 & 0 & 0 & 0 & 0 & 0 & 0 & 0 \\
1.0474 & 0 & 0.8703 & 0 & 0 & 0 & 0 & 0 & 0 & 0 \\
0 & 0.8703 & 0 & 0.6057 & 0 & 0 & 0 & 0.0022 & 0 & 0 \\
0 & 0 & 0.6057 & 0 & 0.5557 & 0 & -0.0732 & 0 & 0 & 0 \\
0 & 0 & 0 & 0.5557 & 0 & 0.6187 & 0 & 0 & 0 & 0 \\
0 & 0 & 0 & 0 & 0.6187 & 0 & 0.5557 & 0 & 0 & 0 \\
0 & 0 & 0 & -0.0732 & 0 & 0.5557 & 0 & 0.6057 & 0 & 0 \\
0 & 0 & 0.0022 & 0 & 0 & 0 & 0.6057 & 0 & 0.8703 & 0 \\
0 & 0 & 0 & 0 & 0 & 0 & 0 & 0.8703 & 0 & 1.0474 \\
0 & 0 & 0 & 0 & 0 & 0 & 0 & 0 & 1.0474 & 0
\end{bmatrix}$$

(a)

$$\begin{bmatrix}
0 & 1.0474 & 0 & 0 & 0 & 0 & 0 & 0 & 0 & 0 \\
1.0474 & 0 & 0.8658 & 0 & 0.0886 & 0 & 0 & 0 & 0 & 0 \\
0 & 0.8658 & 0 & -0.6622 & 0 & 0 & 0 & 0 & 0 & 0 \\
0 & 0 & -0.6622 & 0 & 0.5462 & 0 & 0 & 0 & 0 & 0 \\
0 & 0.0886 & 0 & 0.5462 & 0 & 0.5478 & 0 & 0 & 0 & 0 \\
0 & 0 & 0 & 0 & 0.5478 & 0 & 0.5555 & 0 & 0.0342 & 0 \\
0 & 0 & 0 & 0 & 0 & 0.5555 & 0 & -0.6276 & 0 & 0 \\
0 & 0 & 0 & 0 & 0 & 0 & -0.6276 & 0 & 0.8696 & 0 \\
0 & 0 & 0 & 0 & 0 & 0.0342 & 0 & 0.8696 & 0 & 1.0474 \\
0 & 0 & 0 & 0 & 0 & 0 & 0 & 0 & 1.0474 & 0
\end{bmatrix}$$

(b)

$$\begin{bmatrix}
0 & 1.0489 & 0 & 0 & 0 & 0 & 0 & 0 & 0 & 0 \\
1.0489 & 0 & 0.8682 & 0 & 0.0917 & 0 & 0 & 0 & 0 & 0 \\
0 & 0.8682 & 0 & -0.6670 & 0 & 0 & 0 & 0 & 0 & 0 \\
0 & 0 & -0.6670 & 0 & 0.5567 & 0 & 0 & 0 & 0 & 0 \\
0 & 0.0917 & 0 & 0.5567 & 0 & 0.5532 & 0 & 0 & 0 & 0 \\
0 & 0 & 0 & 0 & 0.5532 & 0 & 0.5615 & 0 & 0.0345 & 0 \\
0 & 0 & 0 & 0 & 0 & 0.5615 & 0 & -0.6380 & 0 & 0 \\
0 & 0 & 0 & 0 & 0 & 0 & -0.6380 & 0 & 0.8723 & 0 \\
0 & 0 & 0 & 0 & 0 & 0.0345 & 0 & 0.8723 & 0 & 1.0489 \\
0 & 0 & 0 & 0 & 0 & 0 & 0 & 0 & 1.0489 & 0
\end{bmatrix}$$

(c)

$$\begin{bmatrix}
0 & 1.0489 & 0 & 0 & 0 & 0 & 0 & 0 & 0 & 0 \\
1.0489 & 0 & 0.6139 & -0.6139 & 0.0917 & 0 & 0 & 0 & 0 & 0 \\
0 & 0.6139 & -0.6670 & 0 & 0.3936 & 0 & 0 & 0 & 0 & 0 \\
0 & -0.6139 & 0 & 0.6670 & 0.3936 & 0 & 0 & 0 & 0 & 0 \\
0 & 0.0917 & 0.3936 & 0.3936 & 0 & 0.5532 & 0 & 0 & 0 & 0 \\
0 & 0 & 0 & 0 & 0.5532 & 0 & 0.3970 & -0.3970 & 0.0345 & 0 \\
0 & 0 & 0 & 0 & 0 & 0.3970 & -0.6380 & 0 & 0.6168 & 0 \\
0 & 0 & 0 & 0 & 0 & -0.3970 & 0 & 0.6380 & 0.6168 & 0 \\
0 & 0 & 0 & 0 & 0 & 0.0345 & 0.6168 & 0.6168 & 0 & 1.0489 \\
0 & 0 & 0 & 0 & 0 & 0 & 0 & 0 & 1.0489 & 0
\end{bmatrix}$$

(d)

FIGURE 11. Coupling matrix obtained during synthesized procedures. (a) Simplified coupling matrix with folded topology synthesized from the Chebyshev filtering function. (b) Topology transformed after coupling matrix rotations. (c) Optimized coupling matrix with coefficients fine-tuning. (d) Final coupling matrix after rotating coefficients M_{23} and M_{67}.

Step 2: Three coupling matrices for states 2 to 4 are resynthesized based on the values of TZs of states 2 to 4 in Table 4 and the return loss of 23 dB.

Step 3: Fine-tune all the coefficients in the coupling matrix using the simplified sweeping-based method. Each coefficient has a dynamic range determined by the corresponding minimum and maximum values in the four matrices. For instance, $M_{12} \in [0.8658, 0.8727]$. It can be observed that the matrices of states 1 and 4 determine the coefficients' dynamic range. All the coefficients in the matrices of states 2 and 3 are within the corresponding range. Therefore, a_2 and a_3 are set to zero, and the constraint on weight factors is simplified to $a_1 + a_4 = 1$. Implementing the sweeping-based method, the final matrix is obtained with weight factors of $a_1 = 0.65$, $a_2 = 0$, $a_3 = 0$, and $a_4 = 0.35$ according to the four matrices corresponding to states 1 to 4, as shown in Fig. 11(c). Repeating steps 1 to 2, the return loss levels and the locations of TZs after fine-tuning coefficients in the matrix are updated in Table 4. The return loss levels of different states are close to each other and are all better than 21.2 dB. The S-parameters and the group delay responses are plotted in Fig. 12(a) and in Fig. 12(b), respectively. As can be seen, the locations of the TZs have a great impact on the filtering characteristics. The more TZs distributed on the imaginary axis of the complex plane, the better the out-of-band suppression is. On the contrary, the more TZs deployed on the real axis of the complex plane, the flatter the group delay is.

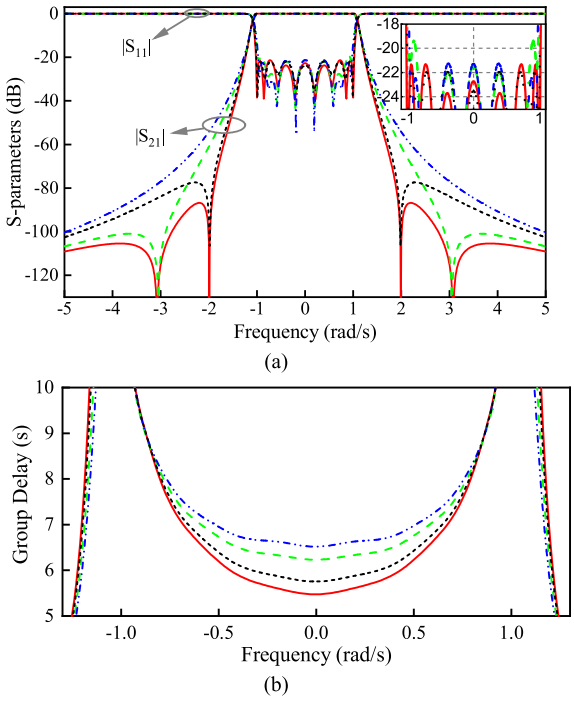

FIGURE 12. Comparison of states after coupling matrix optimization. (a) S-parameters responses after optimization. (b) Group delay responses after optimization corresponding to the curves in Fig. 12(a) using the same color.

Step 4: Repeat steps 1 to 3 until all the states meet the design requirements. Even all the return loss levels are better than 21.2 dB, they are not meet the target. A higher level of return loss can be used to synthesize matrices, such as 25 dB at the beginning. Because the rest of the procedure is very similar, leave it to the readers to complete.

Till now, in the intermediate topology, the responses can be reconfigured by controlling the key coefficients M_{23} and M_{67}. The last step is to rotate the intermediate coupling matrix using (4) and (5). The resultant matrix is given in Fig. 11(d), which is eventually transformed to the quad-section based topology. Now the filter states can be reconfigured by tuning the resonant frequencies of resonators 2, 3, 6, and 7.

V. EXPERIMENTAL VALIDATION

To experimentally validate the proposed theory and techniques, a fourth-order reconfigurable bandpass filter is fabricated and measured. It has two states and both states can be tuned from 9.5 GHz to 10.6 GHz. The filter is initially designed with center frequency of 10.56 GHz and a bandwidth of 300 MHz. It has two symmetric TZs located at ± 4.5j, and

$$\begin{bmatrix} 0 & 1.2176 & 0 & 0 & 0 & 0 \\ 1.2176 & 0 & 1.1175 & 0 & 0.0536 & 0 \\ 0 & 1.1175 & 0 & -0.8387 & 0 & 0 \\ 0 & 0 & -0.8387 & 0 & 1.1175 & 0 \\ 0 & 0.0536 & 0 & 1.1175 & 0 & 1.2176 \\ 0 & 0 & 0 & 0 & 1.2176 & 0 \end{bmatrix}$$

(a)

$$\begin{bmatrix} 0 & 1.2176 & 0 & 0 & 0 & 0 \\ 1.2176 & 0 & 0.7902 & -0.7902 & 0.0536 & 0 \\ 0 & 0.7902 & -0.8387 & 0 & 0.7902 & 0 \\ 0 & -0.7902 & 0 & 0.8387 & 0.7902 & 0 \\ 0 & 0.0536 & 0.7902 & 0.7902 & 0 & 1.2176 \\ 0 & 0 & 0 & 0 & 1.2176 & 0 \end{bmatrix}$$

(b)

FIGURE 13. Normalized coupling matrices corresponding to different topologies. (a) Simplified coupling matrix corresponding to topology in Fig. 1(a) after Chebyshev filtering function synthesis. (b) Rotated coupling matrix corresponding to topology in Fig. 2(b) with angle −0.7854 rad/s.

TABLE 6. Comparison of Filter Performance Before and After Optimization With Related Coefficients and Locations of TZs

No. of States	M_{23}	M_{67}	Return Loss (dB)	Location of TZs
Before fine-tuning coupling matrix coefficients (Before step 3)				
1	-0.6622	-0.6276	23.0000	±2.0000j, ±3.0000j
2	0.5360	-0.6200	20.5050	±1.6042, ±3.0235j
3	-0.6661	0.5760	22.2331	±1.9912j, ±2.7936
4	0.5240	0.5700	20.2532	±1.5882, ±2.7796
After fine-tuning coupling matrix coefficients (After step 3)				
1	-0.6670	-0.6380	21.3203	±1.9901j, ±3.0765j
2	0.5430	-0.6280	21.4306	±1.6022, ±3.0512j
3	-0.6630	0.5920	21.9157	±1.9834j, ±2.8380
4	0.5340	0.5760	21.2592	±1.5904, ±2.8010

the in-band return loss is 28 dB. The choice of a higher level of return loss is mainly done by considering the deterioration of filter performance after the center frequency tuning to a lower frequency.

A. COUPLING MATRIX SYNTHESIS

First, the coupling matrix is synthesized from the generalized Chebyshev filtering function. After simplification, the obtained coupling matrix is shown in Fig. 13(a). The only negative coupling is $M_{23} = -0.8387$, and all the other inter-resonator couplings are positive.

Second, sweep the key coefficient M_{23} to find reconfigurable states by minimizing the cost function in (16). There are two states. One state with the negative value of M_{23} (i.e., −0.8387) is initially synthesized. The other state is found by sweeping the positive values of M_{23}. The value of M_{23} is 0.7840, which gives a return loss of 28.5138 dB. The corresponding return loss performance and locations of TZs with the suitable values of M_{23} are summarized in Table 7. As can be seen, both states meet the design requirements. Therefore, the fine-tuning coefficients in the matrix is not necessary in this example. The final matrix M_F is the same as the initial matrix in Fig. 13(a).

TABLE 7. Corresponding Return Loss Performance and Location of TZs With Suitable Value of M_{23}

No. of States	M_{23}	Solution of s	Return Loss (dB)	Location of TZs
1	0.7840	Pure real	28.5138	±4.2014
2	-0.8387	Pure imaginary	28.0000	±4.5000j

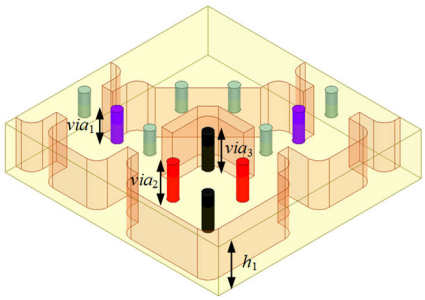

(a)

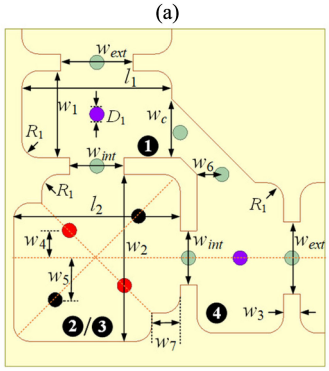

(b)

FIGURE 14. 3-D electromagnetic model of demonstrated bandpass fiter. (a) Perspective view. (b) Top view. Dimensions: $w_1 = 900$, $l_1 = 520$, $w_2 = 1000$, $l_2 = 1000$, $w_3 = 100$, $w_4 = 165$, $w_5 = 250$, $w_6 = 150$, $w_7 = 170$, $R_1 = 100$, $w_{int} = 324$, $w_{ext} = 433$, $w_c = 350$, $h_1 = 400$. Unit: mil.

Third, the mainline coupling M_{23} is rotated by applying (4) and (5) to the coupling matrix in Fig. 13(a). The non-zero coefficients distributed along the diagonal entries of the coupling matrix are shown in Fig. 13(b). Afterwards, to reconfigure the filtering characteristics, the previous internal coupling tuning is completely converted to resonant frequencies tuning.

B. FILTER DESIGN

In this work, a 3D electromagnetic model of the filter is built in the ANSYS High-Frequency Structure Simulator (HFSS). The geometry is shown in Fig. 14. Resonators 1 and 4 are realized as the fundamental modes in two rectangular waveguide cavities, whereas resonators 2 and 3 are realized as dual modes in a large square waveguide cavity. The electric field distribution of the two diagonal modes is simulated by an eigenmode analysis in ANSYS HFSS and shown in Fig. 15. Each diagonal mode is equipped with a pair of tuning screws at the two magnitude peaks. The advantage of this filter is that all the internal and external coupling, no matter positive or negative, are realized through H-plane irises at the center of

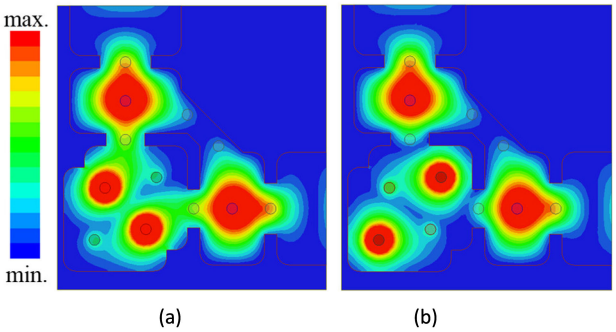

FIGURE 15. **Electric field distribution of two diagonal modes with $via_1 = 93.7$, $via_2 = 170.5$, $via_3 = 169.1$. Unit: mil. (a) Diagonal mode 1. (b) Diagonal mode 2.**

TABLE 8. **Correspondence Between Geometrical Parameters and Coupling Matrix Coefficients**

	Geometrical Parameters	Coupling Coefficients
Fixed parameters	l_1	M_{11}, M_{44}
	w_1	M_{11}, M_{44}
	l_2	M_{22}, M_{33}
	w_2	M_{22}, M_{33}
	w_c	M_{14}
	w_{ext}	M_{12}, M_{34}
	w_{int}	M_{12}, M_{13}, M_{24}, M_{34}, M_{14}
	w_7	M_{22}, M_{33}
Tuning parameters	via_1	M_{11}, M_{44}
	via_2	M_{22}
	via_3	M_{33}

the wall. Tuning screws are provisioned in the cavity where the electric field is the most intensive to tune the resonant frequencies of the corresponding modes. The depth values of tuning screws for the fundamental mode, diagonal mode 1, and diagonal mode 2 in the cavity are defined as via_1, via_2, and via_3, respectively. The tuning screws in the middle of the irises can precisely control the coupling coefficients after fabrication, which are fixed after adjusting coefficients.

The internal coupling irises w_{int} should be deployed in the middle of the wall to consider the performance of each state. To achieve the same internal coupling coefficient for both diagonal modes, two diagonal corner cuts [33], [34] in the square cavity are introduced. The correspondence between geometrical parameters and coupling matrix coefficients is summarized in Table 8. In the model, the fixed parameters are designed first. Then, the tuning parameters are swept to realize reconfigurable states and frequency-tuning performance.

The filter is tuned with the assistance of the synthesized coupling matrix and the help of the model-based vector fitting method [35]–[37]. The simulated and the synthesized coupling matrix responses are plotted together in Fig. 16. According to the synthesized coupling matrix, $M_{22} = -0.8387$ and $M_{33} = 0.8387$ realize a state with TZs on the imaginary axis of the complex plane, and $M_{22} = 0.7840$ and $M_{33} = -0.7840$ realize the other state with TZs on the real axis of the complex plane. In switching between the two kinds of filter

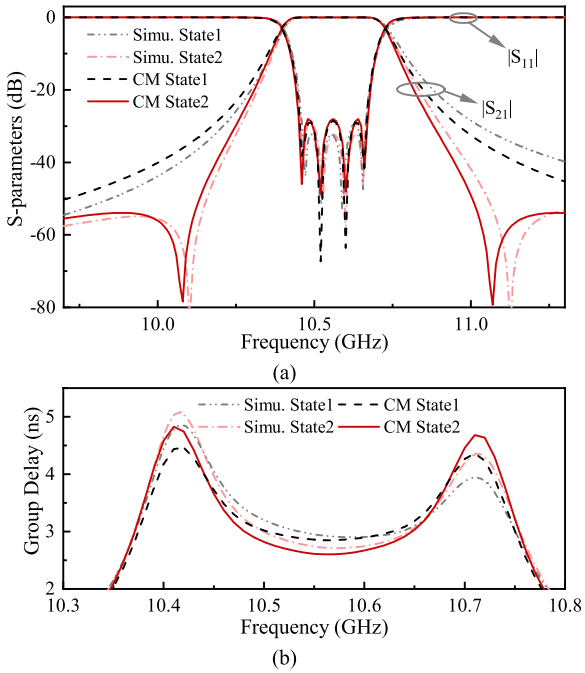

FIGURE 16. **Comparison of states between synthesized coupling matrix and simulated electromagnetic model. (a) S-parameters. (b) Group delay. State1: TZs on the real axis of the complex plane. State2: TZs on the imaginary axis of the complex plane.**

TABLE 9. **The Corresponding Values of via_1, via_2, and via_3 at Different Center Frequencies as Well as States in Fig. 17**

State	f_o (GHz)	via_1 (mil)	via_2 (mil)	via_3 (mil)
state1	10.56	93.7	176.4	163.0
	9.97	138.7	195.1	184.1
	9.50	164.7	210.8	201.1
state2	10.56	93.7	170.5	169.1
	9.97	138.7	190.1	189.2
	9.49	164.7	206.2	205.6

states, all the other coupling coefficients are kept constant. During the simulation, we keep $via_1 = 93.7$ mil and only tune values $via_2 = 176.4$ mil, $via_3 = 163.0$ mil and $via_2 = 170.5$ mil, $via_3 = 169.1$ mil to switch from state1 to state2. It can be seen from Fig. 16(a) that the simulated results are consistent with synthesized coupling matrix states. The group delay responses between the two states given in Fig. 16(b) have a similar enhancement compared to the simulated and synthesized results. Noted that the physical locations of TZs can be deployed closer to the passband by enhancing the coupling between resonator 1 and resonator 4 [23].

Tuning screws via_1, via_2, and via_3 can be used to achieve the tunable performance of this filter. The simulated results of the filter are shown in Fig. 17 and the corresponding values of via_1, via_2, and via_3 at different center frequencies as well as states are given in Table 9. It can be observed that at the same center frequency, the value of via_1 is the same and the states can be switched by changing the values of via_2 and via_3. The frequency-tuning performance of both states can be realized by adjusting the values of via_1, via_2, and via_3 together.

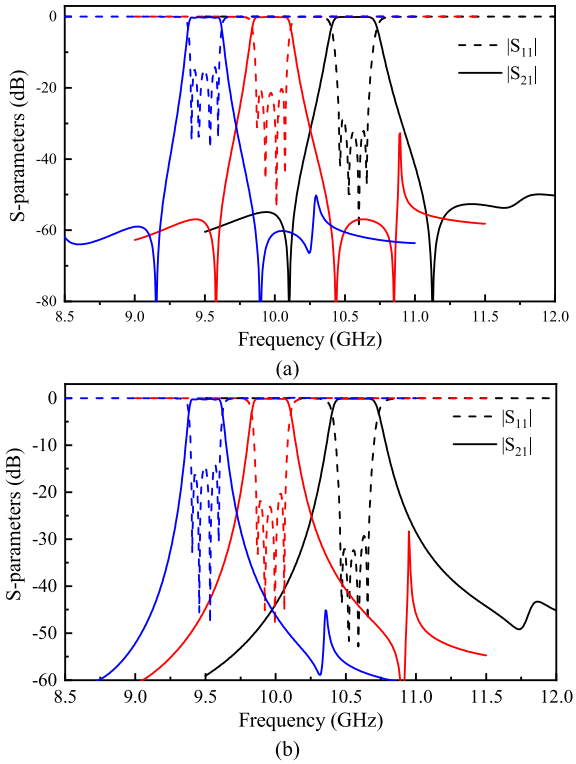

FIGURE 17. Simulated S-parameters responses of the prototyped tunable bandpass filter. (a) Tunable responses of State2. (b) Tunable responses of State1. State1: TZs on the real axis of the complex plane. State2: TZs on the imaginary axis of the complex plane.

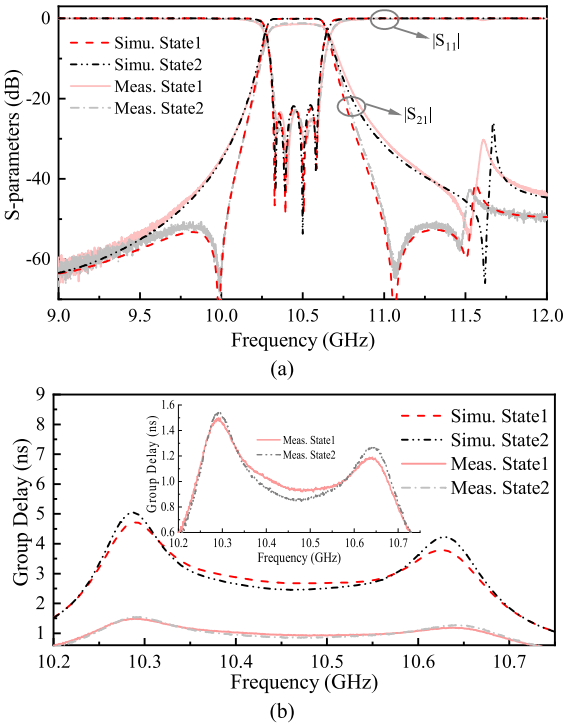

FIGURE 19. Measured responses of the fabricated filter. (a) S-parameters of both states. (b). Measured group delay responses. State1: TZs on the real axis of the complex plane. State2: TZs on the imaginary axis of the complex plane.

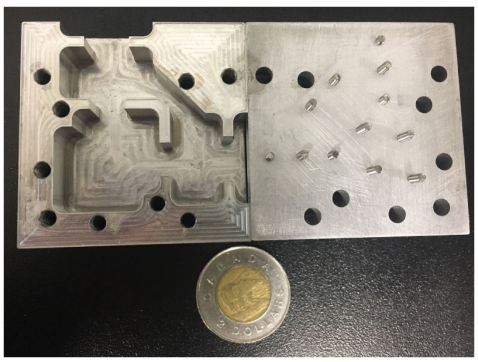

FIGURE 18. Photograph of the fabricated prototype.

Both states have a tuning frequency range from 9.5 GHz to 10.6 GHz. The performance becomes worsen when the resonant frequencies shift far away from the designed center frequency because all the physical coupling irises are fixed, which are set to introduce a mismatch in this scenario. In Fig. 17, there are small peaks on the upper stopband whose magnitude is lower than -28 dB. They result from the spurious resonant modes excited by the tuning screws.

C. FABRICATION AND MEASUREMENT

The photograph of the fabricated tunable bandpass filter is shown in Fig. 18. The filter is made of a piece of aluminium. All the tuning screws are accessible on the top cover. It is measured with a vector network analyzer Keysight N5224A. The measurement results are shown in Fig. 19. The measured bandwidth, insertion loss (IL), and return loss (RL) of the state with TZs on the imaginary axis of the complex plane are 290 MHz, 1.2 dB, and 22.9 dB, respectively, when the filter is tuned to the center frequency of 10.46 GHz. Then, the resonant frequencies of the dual modes can be tuned by changing values of via_2 and via_3. The response is reconfigured to the other state with TZs on the real axis of the complex plane operating at the same band. The IL and RL are 1.5 dB and 23.3 dB, respectively. The peaks beyond the passband in Fig. 19(a) results from the interference modes excited by tuning screws in both states. The group delay curves of these two different states are given in Fig. 19(b), confirming that the TZs on the real axis of the complex plane is beneficial for achieving a better group delay response.

The tunable performances of both states are measured and shown in Fig. 20. The deeper the turning screws are in the cavities, the lower the operating frequency is. The measured tuning ranges of both states are from 9.4 GHz to 10.5 GHz with the insertion loss ranging from 1.2 dB to 2.5 dB. Table 10 provides the comparisons of our work with some other related designs. It can be seen that the tunable performance and reconfigurable filter states (at the same operating frequency) can be realized simultaneously with the same physical structure.

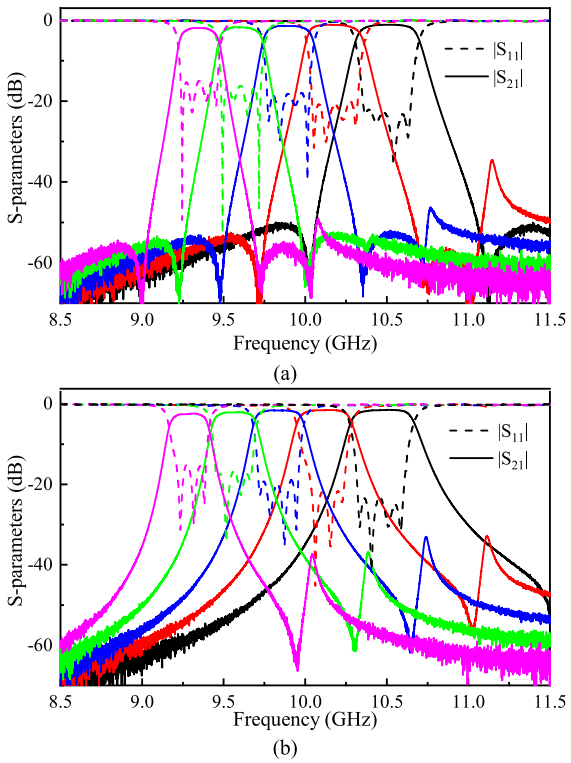

FIGURE 20. Measured S-parameters responses of the tunable bandpass filter. (a) Tunable responses of State2. (b) Tunable responses of State1. State1: TZs on the real axis of the complex plane. State2: TZs on the imaginary axis of the complex plane.

TABLE 10. Comparisons With Other Related State-of-the-Art Designs

Ref.	Type	f_o (GHz)	FBW@ f_o (%)	F-T Range (GHz)	F-T Pct. (%)	Order	No. of TZ	Switchable TZ
[38]	WG	11.5	0.43	11.29-11.68	3.40	4	2	No
[39]	WG	17.37	0.21	17.15-17.59	2.53	4	2	No
[40]	ML	1.19	9.50	0.94-1.44	42.02	2	2	No
[41]	ML	1.22	9.60	0.95-1.48	43.44	4	2	No
[42]	SIW	2.17	3.69	2.00-2.35	16.13	3	2	No
[43]	SIW	2.50	7.20	-	-	4	2	Yes
Ours	WG	9.95	2.91	9.40-10.50	11.06	4	2	Yes

ML: Microstrip Line; SIW: Substrate Integrated Waveguide; WG: Waveguide; FBW: Fractional Bandwidth; F-T: Frequency Tuning; Pct.: Percentage. Ref.: Reference. No. of TZ: Number of TZ.

VI. CONCLUSION

In this paper, the synthesis method for tunable filters with reconfigurable symmetric TZs on the real or imaginary axis of the complex plane has been proposed. The reconfigurable TZs can be realized together with the center frequency control by merely tuning the resonant frequencies of the cavities. The synthesis procedure of these tunable filters for different orders with a variety of coupling diagrams is theoretically interpreted by coupling matrix rotations. The theoretical guidance on reconfiguring symmetric TZs on the complex plane is highlighted because it cannot be directly synthesized through an existing coupling matrix method. Afterwards, the optimization steps for the coupling matrix are given, which make a trade-off among all states' performances of the filter, as demonstrated using a synthesized eighth-order filter. For experimental verification, a fourth-order tunable bandpass filter prototype with a pair of symmetric TZs has been designed, fabricated, and measured. The responses of the fabricated filter can be switched between two states, which has validated the proposed synthesis and design method of the tunable filters. Moreover, this approach can provide a foundation for guiding a flexible design of multi-band and bandstop reconfigurable filters in the future.

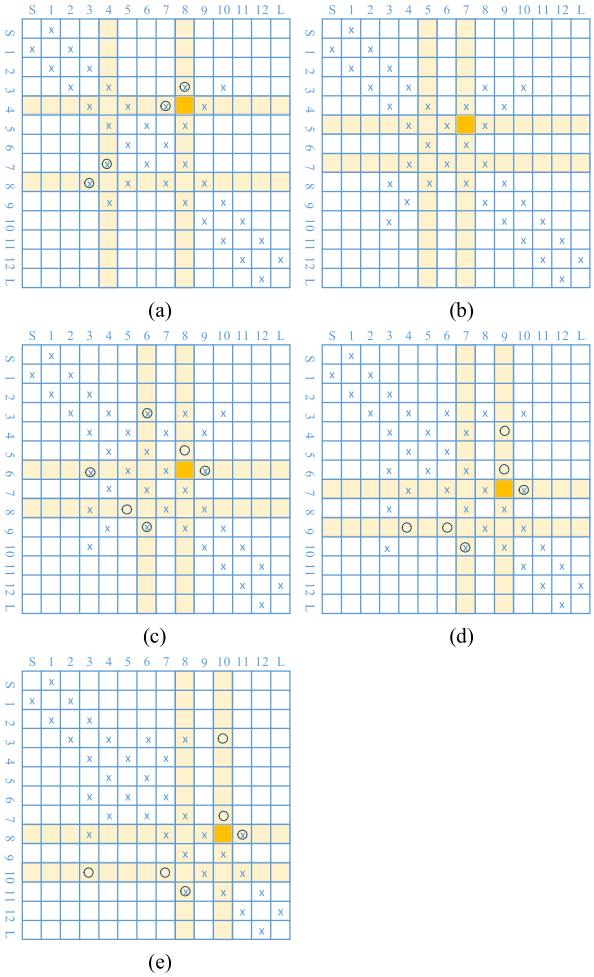

FIGURE 21. Coupling matrix rotations for 12th-order filters. (a) Pivot: M_{48}. (b) Pivot: M_{57}. (c) Pivot: M_{68}. (d) Pivot: M_{79}. (e) Pivot: $M_{8,10}$.

APPENDIX

The procedures of the coupling matrix rotations for a 12th-order filter using a quad-section topology are given step-by-step from the folded configuration. Fig. 21 shows the nonzero entries in the coupling matrix after rotations [16]. The following notations are adopted, such as $c_1 = \cos\theta_1$, $t_1 = \tan\theta_1$, *etc*. After each coupling matrix rotation, the notation M'_{ij} represents the matrix coefficient after the first rotation, *etc*. The details are shown below:

1-1) After the first rotation:

Pivot: M_{48}

$$M'_{34} = c_1 M_{34}$$
$$M'_{45} = c_1 M_{45} - s_1 M_{58}$$
$$M'_{78} = c_1 M_{78}$$
$$M'_{89} = s_1 M_{49} + c_1 M_{89}$$
$$M'_{47} = -s_1 M_{78}$$
$$M'_{49} = c_1 M_{49} - s_1 M_{89}$$
$$M'_{38} = s_1 M_{34}$$
$$M'_{58} = s_1 M_{45} + c_1 M_{58}$$

1-2) After the second rotation:

Pivot: M_{57}

$$M''_{45} = c_2 M'_{45} - s_2 M'_{47}$$
$$M''_{56} = c_2 M'_{56} - s_2 M'_{67}$$
$$M''_{67} = s_2 M'_{56} + c_2 M'_{67}$$
$$M''_{78} = s_2 M'_{58} + c_2 M'_{78}$$
$$M''_{47} = s_2 M'_{45} + c_2 M'_{47}$$
$$M''_{58} = c_2 M'_{58} - s_2 M'_{78}$$

1-3) After the third rotation:

Pivot: M_{68}

$$M'''_{56} = c_3 M''_{56} - s_3 M''_{58}$$
$$M'''_{67} = c_3 M''_{67} - s_3 M''_{78}$$
$$M'''_{78} = s_3 M''_{67} + c_3 M''_{78}$$
$$M'''_{89} = c_3 M''_{89}$$
$$M'''_{58} = s_3 M''_{56} + c_3 M''_{58} = 0$$
$$M'''_{38} = c_3 M''_{38}$$
$$M'''_{36} = -s_3 M''_{38}$$
$$M'''_{69} = -s_3 M''_{89}$$

1-4) After the fourth rotation:

Pivot: M_{79}

$$M^{IV}_{67} = c_4 M'''_{67} - s_4 M'''_{69}$$
$$M^{IV}_{78} = c_4 M'''_{78} - s_4 M'''_{89}$$
$$M^{IV}_{89} = s_4 M'''_{78} + c_4 M'''_{89}$$
$$M^{IV}_{910} = c_4 M'''_{910}$$
$$M^{IV}_{49} = s_4 M'''_{47} + c_4 M'''_{49} = 0$$
$$M^{IV}_{69} = s_4 M'''_{67} + c_4 M'''_{69} = 0$$
$$M^{IV}_{47} = c_4 M'''_{47} - s_4 M'''_{49}$$
$$M^{IV}_{710} = -s_4 M'''_{910}$$

1-5) After the fifth rotation:

Pivot: M_{810}

$$M^{V}_{310} = s_5 M^{IV}_{38} + c_5 M^{IV}_{310} = 0$$
$$M^{V}_{710} = s_5 M^{IV}_{78} + c_5 M^{IV}_{710} = 0$$

c_1, s_1, c_2 and s_2 can be calculated using the above five rotations, and they should satisfy the following conditions,

$$c_2 \left(M'_{38} M'_{910} M'_{49} M'_{56} - M'_{310} b\right) + s_2 \left(-M'_{38} M'_{910} M'_{49} M'_{67} - M'_{310} a\right) = 0$$

$$c_2 s_2 \left[\begin{array}{l} M'_{49}\left(M'^2_{56} - M'^2_{67} + M'^2_{58} - M'^2_{78}\right) \\ -M'_{89}\left(M'_{45} M'_{58} - M'_{47} M'_{78}\right) \end{array}\right] + s_2^2 \left[M'_{49}\left(-M'_{56} M'_{67} - M'_{58} M'_{78}\right) + M'_{89} M'_{45} M'_{78}\right] + c_2^2 \left[M'_{49}\left(M'_{56} M'_{67} + M'_{58} M'_{78}\right) - M'_{89} M'_{47} M'_{58}\right] = 0$$

where

$$a = M'_{45} M'_{56} M'_{78} - M'_{45} M'_{67} M'_{58} - M'_{89} M'_{49} M'_{67}$$
$$b = M'_{47} M'_{56} M'_{78} - M'_{47} M'_{67} M'_{58} + M'_{89} M'_{49} M'_{56}$$

Until now, the first two rotation angles can be calculated using scientific computational tools, such as MATLAB, *etc*. Eliminating M_{811} in the sixth rotation is easy, and the nonzero M_{912} will be created. The remaining steps are similar to the case of an 8$^{\text{th}}$-order filter.

ACKNOWLEDGMENT

The authors would like to thank technical staff S. Dubé from Poly-GRAMES Research Center, Polytechnique Montréal, Montreal, QC, Canada, for fabricating the prototype. The authors would also like to thank Dr. K. Zhou and Dr. J. Xu for the formatting check and modifications.

REFERENCES

[1] S. Adhikari, A. Ghiotto, and K. Wu, "Simultaneous electric and magnetic two-dimensionally tuned parameter-agile SIW devices," *IEEE Trans. Microw. Theory Techn.*, vol. 61, no. 1, pp. 423–435, Jan. 2013.

[2] A. Anand, J. Small, D. Peroulis, and X. Liu, "Theory and design of octave tunable filters with lumped tuning elements," *IEEE Trans. Microw. Theory Techn.*, vol. 61, no. 12, pp. 4353–4364, Dec. 2013.

[3] G. Basavarajappa and R. R. Mansour, "Design methodology of a tunable waveguide filter with a constant absolute bandwidth using a single tuning element," *IEEE Trans. Microw. Theory Techn.*, vol. 66, no. 12, pp. 5632–5639, Dec. 2018.

[4] H. Joshi, H. H. Sigmarsson, S. Moon, D. Peroulis, and W. J. Chappell, "High-Q fully reconfigurable tunable bandpass filters," *IEEE Trans. Microw. Theory Techn.*, vol. 57, no. 12, pp. 3525–3533, Dec. 2009.

[5] M. A. El-Tanani and G. M. Rebeiz, "Corrugated microstrip coupled lines for constant absolute bandwidth tunable filters," *IEEE Trans. Microw. Theory Techn.*, vol. 58, no. 4, pp. 956–963, Apr. 2010.

[6] J. Lee, E. J. Naglich, H. H. Sigmarsson, D. Peroulis, and W. J. Chappell, "Tunable inter-resonator coupling structure with positive and negative values and its application to the field-programmable filter array (FPFA)," *IEEE Trans. Microw. Theory Techn.*, vol. 59, no. 12, pp. 3389–3400, Dec. 2011.

[7] R. Levy, "Filters with single transmission zeros at real or imaginary frequencies," *IEEE Trans. Microw. Theory Techn.*, vol. 24, no. 4, pp. 172–181, Apr. 1976.

[8] J. B. Thomas, "Cross-coupling in coaxial cavity filters - A tutorial overview," *IEEE Trans. Microw. Theory Techn.*, vol. 51, no. 4, pp. 1368–1376, Apr. 2003.

[9] K. T. Jokela, "Narrow-band stripline or microstrip filters with transmission zeros at real and imaginary frequencies," *IEEE Trans. Microw. Theory Techn.*, vol. 28, no. 6, pp. 542–547, Jun. 1980.

[10] S. Amari and U. Rosenberg, "Characteristics of cross (bypass) coupling through higher/lower order modes and their applications in elliptic filter design," *IEEE Trans. Microw. Theory Techn.*, vol. 53, no. 10, pp. 3135–3141, Oct. 2005.

[11] J. D. Rhodes and R. J. Cameron, "General extracted pole synthesis technique with applications to low-loss TE/sub011/mode filters," *IEEE Trans. Microw. Theory Techn.*, vol. 28, no. 9, pp. 1018–1028, Sep. 1980.

[12] M. Yu and Y. Yang, "Unified extracted pole filter synthesis: Bridging the gap between EM and circuit simulations," *IEEE Microw. Mag.,* vol. 21, no. 3, pp. 84–95, Mar. 2020.

[13] L. Szydlowski, A. Lamecki, and M. Mrozowski, "Coupled-resonator waveguide filter in quadruplet topology with frequency-dependent coupling – A design based on coupling matrix," *IEEE Microw. Wireless Compon. Lett.*, vol. 22, no. 11, pp. 553–555, Nov. 2012.

[14] P. Zhao and K. Wu, "Cascading fundamental building blocks with frequency-dependent couplings in microwave filters," *IEEE Trans. Microw. Theory Techn.*, vol. 67, no. 4, pp. 1432–1440, Apr. 2019.

[15] Y. He *et al.*, "A direct matrix synthesis for in-line filters with transmission zeros generated by frequency-variant couplings," *IEEE Trans. Microw. Theory Techn.*, vol. 66, no. 4, pp. 1780–1789, Apr. 2018.

[16] R. J. Cameron and J. D. Rhodes, "Asymmetric realizations for dual-mode bandpass filters," *IEEE Trans. Microw. Theory Techn.*, vol. 29, no. 1, pp. 51–58, Jan. 1981.

[17] S. Tamiazzo and G. Macchiarella, "An analytical technique for the synthesis of cascaded N-tuplets cross-coupled resonators microwave filters using matrix rotations," *IEEE Trans. Microw. Theory Techn.*, vol. 53, no. 5, pp. 1693–1698, May 2005.

[18] G. Macchiarella and S. Tamiazzo, "Synthesis without optimization of cascaded inline prototype filters with arbitrary transmission zeros," in *Proc. 35th Eur. Microw. Conf.*, 2005 pp. 401–404.

[19] R. Levy, "Direct synthesis of cascaded quadruplet (CQ) filters," *IEEE Trans. Microw. Theory Techn.*, vol. 43, no. 12, pp. 2940–2945, Dec. 1995.

[20] X. Chen, W. Hong, T. Cui, J. Chen, and K. Wu, "Substrate integrated waveguide (SIW) linear phase filter," *IEEE Microw. Wireless Compon. Lett.*, vol. 15, no. 11, pp. 787–789, Nov. 2005.

[21] J. D. Rhodes, "The generalized direct-coupled cavity linear phase filter," *IEEE Trans. Microw. Theory Techn.*, vol. 18, no. 6, pp. 308–313, Jun. 1970.

[22] X. Chen and K. Wu, "Substrate integrated waveguide cross-coupled filter with negative coupling structure," *IEEE Trans. Microw. Theory Techn.*, vol. 56, no. 1, pp. 142–149, Jan. 2008.

[23] T. Martin, A. Ghiotto, T. Vuong, K. Wu, and F. Lotz, "Compact quasi-elliptic and highly selective AFSIW filter with multilayer cross-coupling," in *IEEE MTT-S Int. Microw. Symp. Dig.*, 2019, pp. 718–721.

[24] K. Ahn and I. Yom, "A Ka-band multilayer LTCC 4-pole bandpass filter using dual-mode cavity resonators," in *IEEE MTT-S Int. Microw. Symp. Dig.*, 2008, pp. 1235–1238.

[25] W. Shen, X. Sun, W. Yin, J. Mao, and Q. Wei, "A novel single-cavity dual mode substrate integrated waveguide filter with non-resonating node," *IEEE Microw. Wireless Compon. Lett.*, vol. 19, no. 6, pp. 368–370, Jun. 2009.

[26] K. Zhou, C. Zhou, and W. Wu, "Substrate-integrated waveguide dual-mode dual-band bandpass filters with widely controllable bandwidth ratios," *IEEE Trans. Microw. Theory Techn.*, vol. 65, no. 10, pp. 3801–3812, Oct. 2017.

[27] A. Anand and X. Liu, "Reconfigurable planar capacitive coupling in substrate-integrated coaxial-cavity filters," *IEEE Trans. Microw. Theory Techn.*, vol. 64, no. 8, pp. 2548–2560, Aug. 2016.

[28] B. Koh, B. Lee, S. Nam, T. Lee, and J. Lee, "Integration of interresonator coupling structures with applications to filter systems with signal route selectivity," *IEEE Trans. Microw. Theory Techn.*, vol. 64, no. 9, pp. 2790–2803, Sep. 2016.

[29] A. K. Gorur, C. Karpuz, and A. Gorur, "Design of dual-mode dual-band bandpass filter with independently tunable bandwidths and reconfigurable filtering characteristics," in *IEEE MTT-S Int. Microw. Symp. Dig.*, 2017, pp. 922–925.

[30] R. J. Cameron, "General coupling matrix synthesis methods for chebyshev filtering functions," *IEEE Trans. Microw. Theory Techn.*, vol. 47, no. 4, pp. 433–442, Apr. 1999.

[31] R. J. Cameron, C. M. Kudsia, and R. R. Mansour, *Microwave Filters For Communication Systems: Fundamentals, Design, and Applications*, Hoboken, NJ, USA: Wiley, 2018.

[32] P. Zhao and K. Wu, "Circuit model extraction of parallel-connected dual-passband coupled-resonator filters," *IEEE Trans. Microw. Theory Techn.*, vol. 66, no. 2, pp. 822–830, Feb. 2018.

[33] A. Gorur, "Description of coupling between degenerate modes of a dual-mode microstrip loop resonator using a novel perturbation arrangement and its dual-mode bandpass filter applications," *IEEE Trans. Microw. Theory Techn.*, vol. 52, no. 2, pp. 671–677, Feb. 2004.

[34] S. Bastioli, C. Tomassoni, and R. Sorrentino, "A new class of waveguide dual-mode filters using TM and nonresonating modes," *IEEE Trans. Microw. Theory Techn.*, vol. 58, no. 12, pp. 3909–3917, Dec. 2010.

[35] B. Gustavsen and A. Semlyen, "Simulation of transmission line transients using vector fitting and modal decomposition," *IEEE Trans. Power Del.*, vol. 13, no. 2, pp. 605–614, Apr. 1998.

[36] P. Zhao, "Phase de-embedding of narrowband coupled-resonator networks by vector fitting," *IEEE Trans. Microw. Theory Techn.*, early access, Jul. 20, 2018, doi: 10.1109/TMTT.2018.2854170.

[37] P. Zhao and K. Wu, "Model-based vector-fitting method for circuit model extraction of coupled-resonator diplexers," *IEEE Trans. Microw. Theory Techn.*, vol. 64, no. 6, pp. 1787–1797, Jun. 2016.

[38] B. Gowrish and R. R. Mansour, "A dual-mode frequency reconfigurable waveguide filter with a constant frequency spacing between transmission zeros," in *IEEE MTT-S Int. Microw. Symp. Dig.*, 2020, pp. 811–814.

[39] J. Ossorio, J. Vague, V. E. Boria, and M. Guglielmi, "Exploring the tuning range of channel filters for satellite applications using electromagnetic-based computer aided design tools," *IEEE Trans. Microw. Theory Techn.*, vol. 66, no. 2, pp. 717–725, Feb. 2018.

[40] X. Y. Zhang and Q. Xue, "High-selectivity tunable bandpass filters with harmonic suppression," *IEEE Trans. Microw. Theory Techn.*, vol. 58, no. 4, pp. 964–969, Apr. 2010.

[41] D. Tian, Q. Feng, and Q. Xiang, "Synthesis applied 4th-order constant absolute bandwidth frequency-agile bandpass filter with cross-coupling," *IEEE Access*, vol. 6, pp. 72287–72294, Dec. 2018.

[42] B. Lee, S. Nam, T. Lee, and J. Lee, "Third-order frequency-agile substrate-integrated waveguide filter with a pair of transmission zeros," *IEEE Microw. Wireless Compon. Lett.,* vol. 27, no. 6, pp. 566–568, Jun. 2017.

[43] J. Lee, E. J. Naglich, H. H. Sigmarsson, D. Peroulis, and W. J. Chappell, "Tunable inter-resonator coupling structure with positive and negative values and its application to the field-programmable filter array (FPFA)," *IEEE Trans. Microw. Theory Techn.*, vol. 59, no. 12, pp. 3389–3400, Dec. 2011.

WENTAO LIN (Graduate Student Member, IEEE) received the B.Sc. degree in wireless communication and the M.Sc. degree in information and communication systems from Ningbo University, Ningbo, China, in 2013 and 2016, respectively. He is currently working toward the Ph.D. degree in electrical engineering with the École Polytechnique of Montréal, Montreal, QC, Canada. His current research interests include the synthesis and design of reconfigurable microwave components, such as filters and diplexers.

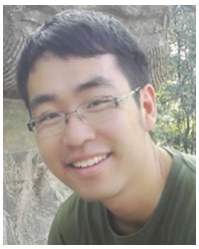

PING ZHAO received the B.Sc. degree from Nanjing University, Nanjing, China, in 2012, and the Ph.D. degree from The Chinese University of Hong Kong, Hong Kong, in 2017. From 2017 to 2019, he was a Postdoctoral Researcher with the École Polytechnique de Montréal, Montreal, QC, Canada. Since 2020, he has been an Associate Professor with the School of Electronic Engineering, National Key Laboratory of Antennas and Microwave Technology, Xidian University, Xi'an, China. His research interests include coupling matrix synthesis techniques for coupled-resonator networks, computer-aided tuning (CAT) for microwave and millimeter-wave filters and diplexers, modeling and optimization of passive RF components, and computer-aided design techniques such as the homotopy method, the artificial neural network, and machine learning techniques.

TAE-HAK LEE (Member, IEEE) received the B.E. degree in electrical engineering from Konkuk University, Seoul, South Korea, in 2007, and the Ph.D. degree in radio communication engineering from Korea University, Seoul, South Korea, in 2015. In 2015, he joined the Research Institute of Computer Information and Communication, Korea University. In 2016, he joined the École Polytechnique de Montréal, Montreal, QC, Canada, as a Postdoctoral Researcher. From 2019 to 2021, he was with Satellite Payload Research and Development Division, Korea Aerospace Research Institute. He is currently an Associate Professor of electronics engineering with Yuhan University, Bucheon, South Korea. His current research interests include reconfigurable/tunable RF and microwave components.

TAIJUN LIU (Senior Member, IEEE) received the B.Sc. degree in electrical engineering from the China University of Petroleum, Dongying, China, in 1986, the M.Sc. degree in electrical engineering from the University of Electronic Science and Technology of China, Chengdu, China, in 1989, and the Ph.D. degree in electrical engineering from the École Polytechnique de Montréal, University of Montreal, Montréal, QC, Canada, in 2005. Following the completion of his doctoral degree, he was a Postdoctoral Fellow with the University of Calgary, Calgary, AB, Canada, for approximately one year. Since May 2006, he has been a Professor with Ningbo University, Ningbo, China. He has authored or coauthored more than 250 technical papers. His research interests include nonlinear modeling and linearization of wideband transmitters/power amplifiers and optical links, and optimization design of ultra-linear high-efficiency intelligent digital transmitters/power amplifiers for broadband wireless communications, RF front-end for cognitive radio system, and radio-over-fiber.

JEAN-JACQUES LAURIN (Senior Member, IEEE) received the B.Eng. degree in engineering physics from Ecole Polytechnique de Montreal, Montreal, QC, Canada, in 1983 and the M.A.Sc. and Ph.D. degrees in electrical engineering from the University of Toronto, Toronto, ON, Canada, in 1986 and 1991, respectively. In 1991, he joined the Poly-Grames Research Centre, Ecole Polytechnique de Montreal, where he is currently a Professor. He is the Co-Director of STARaCom (Center for Systems, Technologies and Applications for Radiofrequency and Communications), a strategic research cluster in the province of Quebec. His research interests include antenna design and modeling, wave processing surfaces, near-field antenna measurement techniques, and electromagnetic compatibility.

KE WU (Fellow, IEEE) is currently the Endowed Industrial Research Chair of future wireless technologies and a Professor of electrical engineering with the École Polytechnique de Montréal (University of Montreal), Montreal, QC, Canada, where he is the Director of Poly-Grames Research Center. He was the Canada Research Chair of RF and millimeter-wave engineering and the Founding Director of the Center for Radiofrequency Electronics Research of Quebec. He held/holds visiting/honorary professorships with various universities around the world. He has graduated more than 74 Ph.D. and 95 M.Sc. Students. He has authored or coauthored more than 1400 referred papers, and a number of books and book chapters and filed more than 50 patents. Dr. Wu was the General Chair of the 2012 IEEE MTT-S International Microwave Symposium, and the 2016 President of the IEEE Microwave Theory and Techniques Society (MTT-S). He was also the inaugural North-American representative in the General Assembly of the European Microwave Association. He was the recipient of many awards and prizes, including the inaugural IEEE MTT-S Outstanding Young Engineer Award, 2004 Fessenden Medal of the IEEE Canada, 2009 Thomas W. Eadie Medal from the Royal Society of Canada, Queen Elizabeth II Diamond Jubilee Medal, 2013 Award of Merit of Federation of Chinese Canadian Professionals, 2014 IEEE MTT-S Microwave Application Award, the 2014 Marie-Victorin Prize (Prix du Quebec), 2015 Prix d'Excellence en Recherche et Innovation of Polytechnique Montréal, 2015 IEEE Montreal Section Gold Medal of Achievement, 2019 IEEE MTT-S Microwave Prize, 2021 EIC Julian C. Smith Medal, and 2022 IEEE MTT-S Outstanding Educator Award. He was an IEEE MTT-S Distinguished Microwave Lecturer. He is a Fellow of the Canadian Academy of Engineering, the Royal Society of Canada, and a member of the National Academy of Science and Engineering of Germany.